Impact of Turning-Induced Shape Deformations on Aerodynamic Performance of Leading Edge Inflatable Kites

Master Thesis

Shivaang Sachdeva

Technische Universiteit Delft

TU Delft Delft University of Technology

Challenge the future

Impact of Turning-Induced Shape Deformations on Aerodynamic Performance of Leading Edge Inflatable Kites

Master Thesis

by

Shivaang Sachdeva

in partial fulfillment of the requirements for the degree of

Master of Science
in Aerospace Engineering

at the Delft University of Technology,

Student number: 4092805
Supervisor: Dr. -Ing. R. Schmehl
M. Folkersma, MSc

TU Delft Delft University of Technology

Contents

Summary

With growing energy demands and a need to switch to a sustainable source of energy key stakeholders are considering the use of high altitude wind energy systems. TU Delft and its start up company kitepower are key stakeholders investigating the commercial viability of this technology. With this goal the research group has developed several kite systems capable of accessing high altitude winds. It is believed that the low investment cost and high performance of kites could lead to a lower cost of energy. Concepts currently being considered involve a leading edge inflatable (LEI) kite that is controlled by an on-board control unit and is connected to a ground-based generator. Once the kite is deployed to the required altitude it enters a power generation stage where it is flown in a figure eight routine. This routine is controlled by the on-board control unit that pulls on tethers that are connected to the tip of the kite. This process is followed by a retraction phase where the kite is pulled back in. The goal of the system is to maximize energy production in the generation phase while limiting the energy consumed in the retraction phase. It is critical to assess and improve the kite design and its performance at all stages of operation such that the net power production can be maximized. While significant advancements have been made into the performance for normal flight there is a lack of research on the aerodynamic performance when there is control input to initiate a turn.

The shape of the kite and the high angle of attack at which the kite is flown results in complex flow behavior involving separation, flow vortices, flow reattachment etc. This poses several challenges to maintain accuracy. A computational approach involving a steady-state Reynolds-averaged Navier Stoke (RANS) simulation is believed to be a computationally viable mode of analysis to capture the flow behavior. This thesis details the approach used to improve results attained using this method and understand the influence of deformations associated with control inputs on the aerodynamic performance of the kite.

A control input is simulated using a finite element model (FEM) with the Abaqus software by reducing the length of the right steering and increasing the length of the left steering line by 0.5 m. This results in the right side reducing its curvature and being pulled towards the kite control unit (KCU). Whilst on the left side the bridle lines are less tensed, leading to an increase in curvature. The turning performance is governed by the offset and variations in magnitudes of forces.

Meshes are generated that attempts to minimize geometry alterations whilst still maintaining high quality. The influence of boundary layer parameters are investigated. A trade-off is made where the influence of key parameters on accuracy and computational time is evaluated; where applicable improvements are made. Both the global as well as the local parameters of the kite in normal as well as turning orientation are analyzed. The results show that control induced deformations lead to a percentage reduction in the lift, whilst the effect on the drag is minimal. It is further seen that the kite initiates stall at an angle of approximately 40 degrees. The stall behavior is initiated at the mid-span of the kite and gradually moves to the tip. The turning performance is measured by looking at the yaw moment. The magnitude of this parameter is linked to the offset and magnitude in force vectors at the tip. Due to the delayed stall at the tips, it is observed that the yaw moment increases beyond 40 degrees.

Accuracy issues using this method were seen when performing a validation study on a profile similar to that of the kite. These issues could be due to limitations of the method or potential errors in the reference study. It is recommended to reevaluate the validation study before using this method for detailed flow analysis.

It is concluded, that in order to fully trust the relevance of the results, one would have to have to conduct a validation study. However the method's ability to address non-linear flow effects within a limited time frame makes it a viable option for design optimization/system modelling.

Acknowledgements

Prima facea, I am grateful to God for good health and well-being that were necessary to complete this thesis. The support that He has provided allowed me to strive ahead when most vulnerable.

This thesis accumulates and presents the knowledge that I have attained in my studies. The blood, sweat and tears that have gone in the fulfillment of this milestone is something that I will not forget for the rest of my life. I would not be here without the support of my family, friends, teachers and professors.

I would firstly like to thank my thesis supervisors Dr. -Ing Roland Schmehl and Mikko Folkersma, MSc. The door to Prof. Schmehl's office was always been open whenever I ran into problems or had questions about my research. He has consistently provided the support, motivation and constantly steered me in the right direction. I would like to equally thank my daily supervisor Mikko Folkersma, he has also been there to provide technical knowledge and support when required. The discussions I have had with him have guided me to the completion of this thesis.

I would like to thank the Enervate team, that allowed me to participate in kite testing and personally see the growth in this field. I hope you excel in this area and meet the expectations and goals you set out to achieve with this technology.

A special thank goes to Mr Roland Verheul, he provided me with the models that were a basis of the study and has helped me understand the topic in greater detail. Whilst his schedule was very busy, he was able to find the time to help a student with whom he had no direct affiliation.

Whilst I have not personally met him, I would also like to thank Michael Deaves. His work has been the basis for this thesis. The well documented approach and results was useful in the overall assessments made in this thesis.

I would like to also thank my friends for their help and support in helping me procrastinate. Without them I would have gone through my studies without the satisfaction of truly enjoying my life as a student.

Finally, I must express my very profound gratitude to my parents and brother. They have provided me with support both financially and emotionally that I have required throughout my life. The care that I have received from them has allowed me to be the individual that I am today.

List of Figures

List of Tables

Nomenclature

Acronyms

AWE	Airborne Wind Energy
DNS	Direct Numerical Simulation
FEM	Finite Element Model
FVM	Finite Volume Method
KCU	Kite Control Unit
LEI	Leading Edge Inflatable
LES	Large Eddy Simulation
LLT	Lifting Line Theory
RANS	Reynolds-Averaged Navier-Stoke
VLM	Vortex Lattice Method
SIMPLE	Semi-Implicit Method for Pressure Linked Equations
SST	Shear Stress Transport
TU Delft	Technical University of Delft
V2	Mutiny Optimized Kite

Greek Symbols

α	Angle of Attack	deg
α_t	Local Section Twist	deg
β	Turbulence Model Constants	-
Γ	Dihedral Angle	deg
γ	Turbulence Model Constants	-
Δ	Boundary Layer Height	m
δ_{ij}	Kronecker Delta	-
ϵ	Turbulent Dissipation Rate	m^2/s^3
μ	Dynamic viscosity	kg/ms
μ_t	Eddy Viscosity	m^2/s
ρ	Density	kg/m^3
σ_k	Turbulence Model Constants	-
σ_ω	Turbulence Model Constants	-
$\tau_{t_{ij}}$	Reynolds stress	$kg \cdot s^2/m$

τ_w	Wall Shear Stress	kg/ms^2
υ	Kinematic viscosity	m^2/s
ω	Specific Turbulent Dissipation Rate	1/s

Roman Symbols

a	Adiabatic Lapse Rate	K/m
AR	Aspect Ratio	-
b	Wing Span	m
c_{avg}	Mean Aerodynamic Chord	m
C_D	3D Drag Coefficient	-
C_f	Skin Friction Coefficient	-
C_L	3D Lift Coefficient	-
c_μ	Model Coefficient	-
D	Drag Force Vector	m/s
d/c	Diameter to Chord Ratio	-
f_μ	Damping Function	-
g_0	Acceleration due to Gravity on Earth Surface	m/s^2
h	Height	m
k	Turbulent Kinetic Energy	m^2/s^2
L	Lift Force Vector	kg · m/s
l	Characteristic Length	m
p	Pressure	kg/ms^2
Pe	Peclet Number	-
Re	Reynolds Number	-
S	Characteristic Area	m^2
Sc_t	Turbulent Schmidt Number	-
S_{ij}	Mean Velocity Strain Tensor	1/s
t	Time	s
T	Temperature	K
$\mathbf{T}_t$	Traction Force Vector	kg · m/s
U	Wind Velocity	m/s
u^τ	Friction Velocity	m/s
$\mathbf{U}_i$	Flow Vector	m
$\mathbf{V}_a$	Apparent Wind Velocity Vector	m/s
$\mathbf{V}_C$	Cross Wind Velocity Vector	m/s

$\mathbf{V}_k$	Kite Velocity Vector	m/s
$\mathbf{V}_w$	Wind Velocity Vector	m/s
$\mathbf{x}_i$	Directional Vector	m
y^+	Non-Dimensional Wall Parameter	-
z_0	Surface Roughness	m

1

Introduction

1.1. Airborne Wind Energy

From the start of the industrial revolution, economic growth has largely been linked to energy consumption. It is predicted by International Energy Agency [23] that the demand for energy is going to increase by one-third from 2013 to 2040 with electricity demand increasing by 70% . Conventional modes of energy generation such as the burning of coal and oil release the by-product carbon dioxide (CO_2), which is causing a phenomenon of global warming. If current trends continue the impact on the planet will lead to drastic implications on societies around the world [36]. Considering this, a majority of countries have pledged to reduce their carbon footprint and make a global effort to tackle this issue in the recent Climate Summit in Paris [50]. Initiatives to attain the goals of the summit include increasing renewable energy's contribution in the energy sector. An estimate by the International Energy Agency in 2015 predicted that with a collaborative effort renewable energy will take over coal as the largest source of electricity by 2030 [23].

A major source of renewable energy is the wind sector, contributing 3.1% of total electricity production by the end of 2014, making it the second most in terms of renewable sources after hydropower [40]. The wind energy sector has seen a massive growth in recent years and with recent developments is turning out to be the cheapest source of energy in many high wind locations. A challenge for this sector is the limited onshore high wind locations. This has been tackled partially with the expansion offshore. Although construction offshore requires much more investment, one is able to make up for it with higher power production due to greater wind speeds. A key challenge with offshore technologies is to make it commercially viable as one moves further from land. The increasing depth of water bodies leads to a larger substructure, higher cable losses, higher cost of construction and maintenance. In an effort to tackle this the capacity and scale of the turbines are being increased. This however poses multiple challenges, with transportation and aeroelasticity. The industry believes that unless sufficient advancements are made in the area of floating substructures the commercial scope of this technology is highly limited [4]. Alternate technologies such as airborne wind energy (AWE) systems are being considered as an option to tackle this issue. AWE systems are capable of using the high and persistent wind speeds that are blowing at altitudes higher than ones attainable by conventional turbines. Furthermore, the aerodynamic shape of the geometry can be maintained for the full span of the kite; which is not the case for traditional turbines where as one goes towards the root of the blade the thickness increases. Majority of the systems currently being considered attempt to use highly aerodynamic kite designs that can attain the required altitude with a limited support structure. This offers a low initial investment opportunity along with a high power potential and is extremely useful for areas where transport and construction is difficult.

A significant section of the AWE systems currently being researched employ design modifications towards toy kites such that aerodynamic performance can be maximized. Kites have traditionally been used to access extreme altitudes for meteorological data gathering. In this effort, kites were designed to optimize stability and have the ability to carry the payload required for meteorological studies. This approach initially lead to the addition of dihedral to the conventional diamond toy kites for stability, and consequently towards a box configuration to increase the payload capacity [1]. During

this period research was conducted by Ito and Komura [22] regarding mechanisms that cause the kite to become unstable. The research noted twisting, asymmetrical areas, uneven tension of construction material and changes in bridle point locations as key factors influencing instability and attempted to find ways in which it could be restricted. With the advent of surf and traction kites, the focus has shifted towards kite designs with high maneuverability. With this in mind Stevenson looked into factors that influence maneuverability. Two key indicators were identified namely the yaw moment and the lateral movement [48]. Subsequent tests were carried out on a simple rigid box kite to assess the impact of key parameters such as level of dihedral/anhedral, yaw angle and roll angle on the moment coefficients of the kite. The research provides basic insight into the turning mechanisms and suggested ways in which turning performance can be enhanced. The suggestions included having an anhedral shape and connecting the bridle lines at the tips of the kite. One can see this structural change in current traction kite and surf-kite designs wherein the control lines are situated at the trailing edge tip of the kite and a shift from dihedral orientation to anhedral [48].

1.2. TU Delft Concepts

Technical University of Delft (TU Delft) has taken an active part in researching the field of AWE systems. They have developed, optimized and compared multiple different concepts. Controllability has been a key challenge associated with the research and has contributed to discarding several concepts. Given below is a list of concepts that have been developed by TU Delft and how they performed.

1. **Ram-air kite**: The initial design of TU Delft involved a ram-air kite, using the off-shelf Peter Lynn Kite. It was controlled using steering rails at the tip and a kite control unit system. This system however was not successful as the bridle lines twisted and the steering mechanism jammed [9].

2. **Kiteplane**: The kiteplane design is a self-design project of Breukels and Ockels [10]. The goal initially was to achieve the highest altitude for a flying kite and was first conceptualized in 2003. The initial design involved a foam based structure, which had very low drag. It lacked sufficient durability, transportability, scalability and was highly volatile in control (due to its low drag). The subsequent version was scaled and built to be inflatable (to allow transportation). This concept was further optimized externally, and the third model was introduced. This model involved a scale up and reduction in pressure drag. Controllability and aeroelastic phenomenons ultimately led to the abandonment of the concept.

3. **Leading Edge Inflatable Kites**: Recently TU Delft has been focusing on the development of LEI kites due to their large depower range, they started from off the shelf products and have been optimized through flight tests and knowledge gained [1]. The initial design involved a scaled version of the surfkite design of Mutiny. Following flight tests it was realized that additional reinforcements would be required. In this regard the second iteration was introduced, with additional struts and adaptions to the leading edge. Furthermore, the bridle connection was changed. [8]

   An additional LEI design was also created using the off-shelf Genetrix Hydra surfkite design. It is more slender and has a higher depower range. This design is smaller and suitable for high wind conditions. Furthermore, it has a complex trailing edge as compared to the Mutiny designs. This design was optimized and scaled up for version three of the LEI kites. The shape of the leading edge has been optimized to have a billowed shape [18]. Currently, research is ongoing for a design having a carbon-fiber leading edge. Carbon fiber has good structural properties and would be able to achieve the same stiffness with a slender leading edge. Furthermore, the new design has been optimized by having fewer struts, thereby optimizing aerodynamics.

Currently, there are four main designs that are being used for system tests namely the Genetrix Hydra, Optimized Genetrix Hydra (V3), Mutiny optimised (V2) and a carbon fiber leading edge kite. One can view the different TU Delft designs in Figure 1.1. Furthermore, one can see the whole assembly of a LEI kite in Figure 1.2. This study will focus on the Mutiny optimized (V2) due to its simplistic design.

1.3. TU Delft kite system

The V2 kite system involves a LEI kite attached to the KCU (control pod) with multiple bridle lines as shown in Figure 1.2. The bridle lines are attached to the leading edge of the kite and used to control

Figure 1.1: Different TU Delft concepts, top left: Ram-air, top right: kiteplane, bottom left: LEI (V2), bottom right: LEI (V3) [18]

the structural shape and orientation of the kite. Specific bridle lines can be pulled to change the kite's angle of attack (power lines) or to initiate a turn (control lines). The power lines are attached to key points along the leading edge to ensure limited local deformations thereby maintaining the shape of the kite. The control lines on the other hand are attached to the tips of the kite to maximize the moment arm for the turn. The bridle use multiple pulleys to control the length of key bridle lines required by the maneuver.

The KCU is connected to a ground generator using a single tether. This tether is pulled by the kite to generate power. In order to maximize the power one has to maximize the pull force. This is achieved by orienting the kite perpendicular to the wind (crosswind orientation) shown by the blue dot in Figure 1.3. The velocities and forces experienced by the kite in this orientation can be seen in Figure 1.4. One can see that for this case the kite velocity $\mathbf{V}_k$ ($\mathbf{V}_C$ in figure) is perpendicular to the wind velocity $\mathbf{V}_W$ leading to the highest apparent velocity $\mathbf{V}_a$. Due to symmetry between the forces triangle (Lift (**L**) and Drag (**D**)) and the velocity triangle one can derive the crosswind velocity equation 1.1, where $(L/D)_k$ is dependent on the kite aerodynamics. The lift is formulated using equation 1.2 where C_L is the kite's lift coefficient, ρ is density and S is the characteristic area. By making the assumptions that the kite velocity is crosswind (V_k=V_C), the lift force is equal to the traction force ($L = T_t$), weight of kite can be neglected and by neglecting bridle and tether drag; one can get Loyd's expression for the idealized power production shown in equation 1.3 where C_D is the drag coefficient [26] [1]. One can see that the power has a cubic relationship with the wind velocity and for the best performance the aerodynamics of the kite should maximize $\frac{C_L^3}{C_D^2}$.

$$V_c = (V_W - V_L)(L/D)_k \tag{1.1}$$

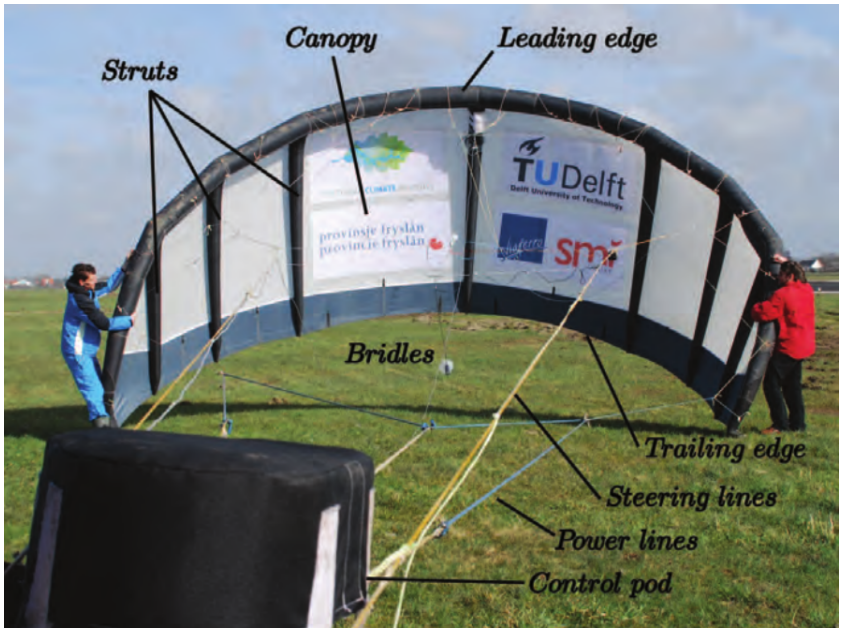

Figure 1.2: Naming convention for the different parts of a kite [8]

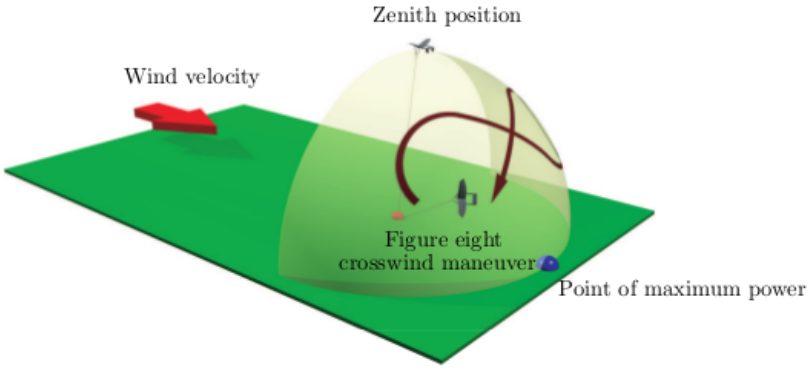

Figure 1.3: Crosswind wind window [9]

$$L = 0.5 C_L \rho V_a^2 S \tag{1.2}$$

$$P = \frac{2}{27} \rho S V_w^3 C_L \left(\frac{C_L}{C_D}\right)^2 \tag{1.3}$$

The operation phase of the kite involves two stages namely the generation and retraction phase. In the generation phase the aforementioned equations are applied to maximize power production and in the retraction phase the kite is pitched out and reeled back in. One can visualize this in Figure 1.5. The goal of a kite system is to maximize the efficiency in the generation phase whilst minimizing the time in the retraction phase [8]. In this regard a study was conducted where key points were selected based on their elevation and azimuth, these were used as alternating attraction points for the kites motion. At high elevation angles it was found that the figure eight approach produced the shortest path for the kite. It was seen that for high winds the uploop figure eight pattern produced a constant and easy to control cable tension [1]. The kite is therefore maneuvered to follow this trajectory. This motion results in a power production cycle shown in Figure 1.6. When the power is negative the system is in retraction phase and uses energy to pull the kite back. The net gain is the power produced by the system.

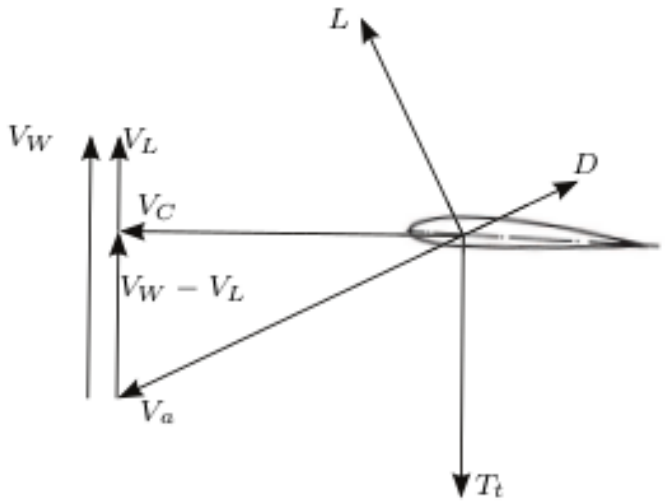

Figure 1.4: Crosswind wind forces and velocities [9]

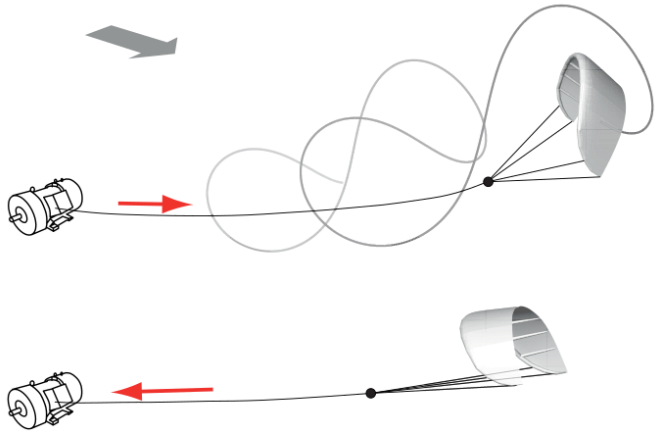

Figure 1.5: Kite power cycle: figure 8 maneuvers to generate power followed by a retraction [8]

For the operation stage, the kite is flown at significantly high angle of attacks for optimal aerodynamics. From Figure 1.7, one can see that the kite typically operates at an angle of attack between 20 to 50 degrees with a mean of approximately 35 degrees. There is however a concern that the angle of attack might not be accurately measured in this analysis as the sensor might not be positioned at the mean chord line (chord length varies with span). One can also see the side-slip angle (angle between the wind and the kite frontal area) varies between -15 and 15 degrees depending on whether it is a right or a left turn.

The figure eight movement is controlled by the KCU system. This system allows the contraction/extension of the steering lines that are connected to the tip of the kite. By pulling the steering line the local angle of attack of the kite (on the side that the line is pulled) increases causing an increase in local lift and drag. Apart from the change in local angle of attack the side that is pulled also deforms such that the tip moves forward, this leads to an offset in the forces at the tips. By comparing the turning behavior of a rigid to a flexible kite Breukels confirmed [9] that the yawing moment is largely contributed from the offset in tip forces. One can see the deformations associated with a right tip control input in Figure 1.8 (for further detail refer to Appendix C3 in reference [8] which shows the deformation associated with a Rhino kite for a figure 8 maneuver).

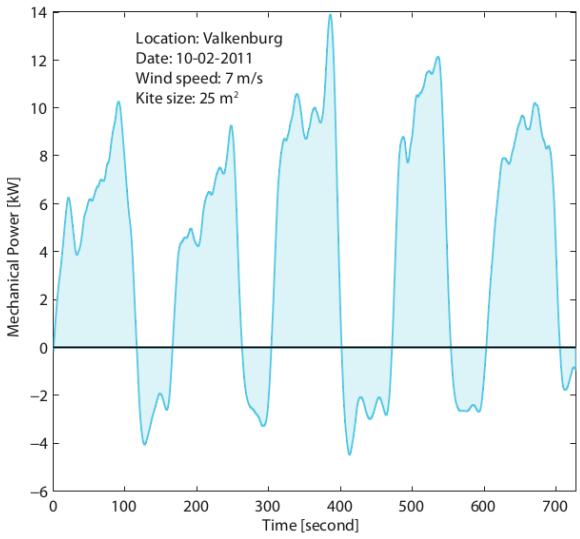

Figure 1.6: Power produced by kite at Valkenburg [8]

1.4. Thesis Objective

By understanding the behavior of the kite at all stages of operation, the TU Delft research team will be able to better understand and predict the behavior of the kite in its environment. With this it would be possible for the TU Delft kite team to develop better design for the future. The basis of this thesis will be the work of Deaves [15]. His thesis attempts to understand the 3D flow behavior of the TU Delft V2 kite at different angles of attack. The thesis performs a 3D flow analysis using Computational Fluid Dynamics (CFD) for the V2 kite. The thesis has three key goals:

1. The first goal is to improve the mesh of Deaves [15] by limiting geometry alterations considered and reducing meshing errors. This will improve the accuracy of results along with the computation time of the simulations.

2. The second major goal of the thesis will be to understand the turning behavior of the kite. This will involve developing a model for the kite with a control input, and assessing key aerodynamic parameters. The study will look at both global as well as local aerodynamic parameters.

3. The third goal of this thesis is to investigate if this modelling approach is capable of addressing the flow of the kite and can be used for further development with regards to the design of the kite.

The thesis will be divided into three major chapters. The first chapter will perform a literature review which will look at the kite system and modeling techniques to analyze the kites aerodynamics and structure. The second chapter will cover the setup of the CFD model that will be used to analyze the kite's aerodynamics. The third chapter will present and analyze the results of the simulation. The conclusions will then offer a summary of the results and the relevance they have in current research regarding kites, and recommendations will be made on potential areas for future research.

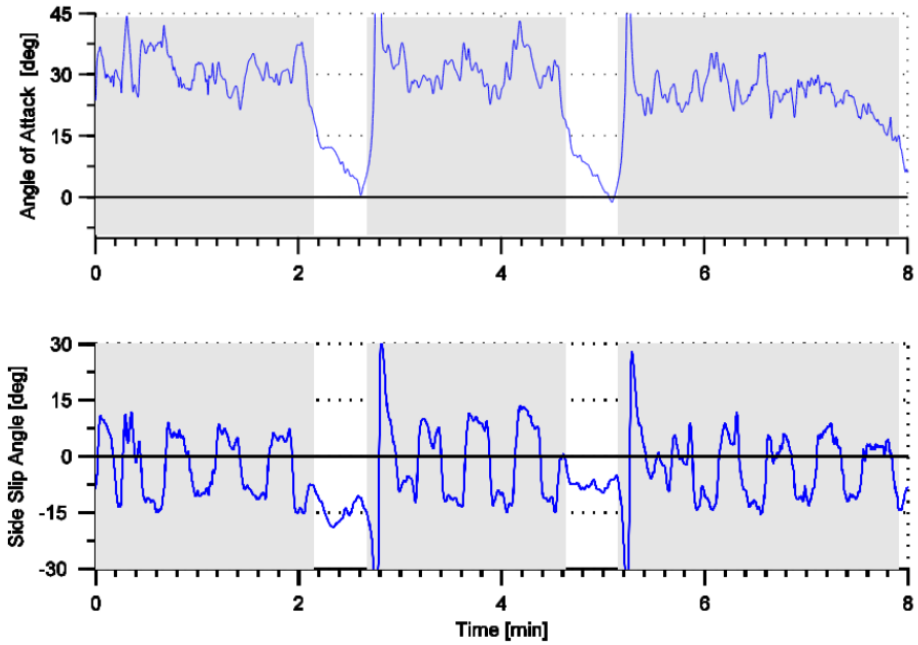

Figure 1.7: Angle of attack and side slip angle during a kite test [43]

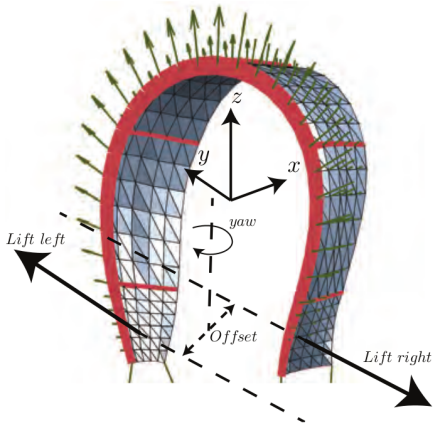

Figure 1.8: Deformations due to control input [8]

2

Kite Modelling

This chapter consists of a literature review looking at the TU Delft Mutiny V2 kite and the environment in which it functions. It will further discuss the different models that are used to analyze the structural and aerodynamic properties of kites. This will develop a basis of the method that will be used for the aerodynamic simulation of the kite.

2.1. Kite and its Environment

The kite that will be used for the analysis and that is still in operation at TU Delft is the Mutiny V2. This kite as shown in Figure 1.2, is a LEI kite with a KCU that controls the kite. The kite has a flat surface area of $25m^2$ and is divided into eight spanwise sections separated by struts. The leading edge and the struts are used to provide structural rigidity and shape to the canopy. The kite is connected to the KCU using bridle lines which are used to control the kite shape and maneuver the kite. The kite has a curved shape with the middle section having the highest chord length which reduces to zero at the tips. The kite has a flat wing span (b) of 10.7m and an Aspect Ratio (AR) of 4.58 [24], leading to a mean aerodynamic chord length c_{avg} of 2.34 m ($AR = \frac{b^2}{S} = \frac{b}{c_{avg}}$).

The kite operation is limited to a height of 700m and is generally bounded by an altitude of 150m-500m [15]. The environmental conditions at this level (tropopause) can be estimated by the adiabatic lapse rate ($a = -0.0065\frac{K}{m}$ in the tropopause) which is a proportional term that describes the relation between temperature at the ground ($T_0 = 288.15K$) and at an altitude (T_1) using equation 2.1, where $h_0 - h_1$ is the altitude. One can then use the temperature relationship and the standard sea level conditions ($p_0 = 1.013 \times 10^5 Pa$, $\rho_0 = 1.225\frac{Kg}{m^3}$,$g_0 = 9.81\frac{m}{s^2}$) to get the pressure and density at the required altitude (h_1) using equations 2.2 and 2.3, reproduced from [2]. At an altitude of 300m (a close estimate of the altitude of the kite) one gets that the temperature is 286K, the pressure is 9.8×10^4 Pa and the density is 1.19 Kg/m^3.

The wind velocity, on the other hand, varies with location and cannot be governed by standard conditions. It is governed by the uneven heating due to the sun (which varies both in time and by location), irregularities in the earth's surface and boundary layer impact of the earth's surface. As one goes to a higher altitude the distance between the surface is greater, leading to a limited boundary layer impact and a higher velocity. In order to quantify this one can use the logarithmic law. This law given by equation 2.4 relates the surface roughness (z_0) and the wind velocity at a reference height (U_{ref}) to the wind velocity at the required altitude. The surface roughness is a parameter used to characterize the surface topology at the given location, for example, an open landscape has a value of 0.1 m and a rough landscape has a value of 0.2 m. When considering heights greater than the boundary layer (meso height) one has to resolve the equation twice. Therefore to approximate the wind speed at a height greater than 60m (approximate meso-height) one has to firstly use equation 2.4 to get the wind speed at 60m and then use this as a reference height to compute the velocity at a higher altitude [49].

One can approximate the velocity that the kite faces as being between 20m/s to 45 m/s, this was encountered in a flight test conducted in Valkenburg on June 2012 [15]. As this velocity is lower than a Mach number of 0.3, the flow can be assumed as incompressible without making significant errors.

Based on these environmental parameters the Reynolds number (Re) of the kite is computed to be in the range of 3.04×10^6 to 6.83×10^6 using equation 2.5, where l is the characteristic length and μ is the dynamic viscosity. For this study the Reynolds number will be taken as 6×10^6 to allow for comparison's with the results of Deaves [15].

$$T_1 = T_0 + a(h_1 - h_0) \tag{2.1}$$

$$\frac{p_1}{p_0} = \frac{T_1}{T_0}^{-\frac{g_0}{a*R}} \tag{2.2}$$

$$\frac{p_1}{p_0} = \frac{T_1}{T_0}^{-\frac{g_0}{a*R}} \tag{2.3}$$

$$U_1 = U_{ref} \frac{ln(\frac{h}{z_0})}{ln(\frac{h_{ref}}{z_0})} \tag{2.4}$$

$$Re = \frac{\rho U l}{\mu} \tag{2.5}$$

2.2. Structural Models

The structure of the kite can be modelled in multiple ways. The methods vary by the degrees of freedom and the accuracy. Having a higher degree of freedom will generally lead to higher accuracy but would lead to a higher computation time. Given below are a list of structural models that have been used to analyze kites.

1. **Black Box Model**: The black box model works by fitting mathematical models to experimental data. The advantage of such a system is that it predicts the behaviour of the kite exactly as in experiments. The model is however only valid if the simulation is done with the exact same parameters as the experiment. The model is also not useful to compare new designs and offers no insight and reasoning to the results [15].

2. **Point Mass Model**: This model approximates the kite as a point where the different forces such as lift and drag are assumed to be a point force that can be computed using a flat plate model. The dynamics including flexibility are ignored and estimates for direction and magnitude of forces are computed based solely on the pitch and yaw angle. It produces results quickly however offers very limited information and uses assumptions that are unrealistic leading to severe accuracy issues. Its fast speed however makes it useful for preliminary studies into trajectory optimization and system performances [8].

3. **Rigid Body Model**: This model increases the degrees of freedom by including attitude dynamics of the kite. One can therefore simulate, the kite's translational as well as rotational motion (i.e. 6 degrees of freedom). The body is rigid and is not flexible but the arc shaped geometry can be added. This model is similar to those used for airplanes and therefore there is ample literature and analysis of this method. This method has been used by de Groot in his model [14] however it was concluded that without the modelling of flexibility the dynamics of the kite will not be realistic [9].

4. **Multi-Plate Model**: In this model multiple plates are connected using imaginary hinges to form the kite. The forces are determined using plate theory separately. This model includes some deformations but the deformations do not include the complete flexibility of the kite, furthermore as the actual kite does not have hinges and springs the model requires fictitious forces and is not accurate at modeling the deflections [15].

5. **Lumped Mass model**: In this model the kite structure is described by multiple lumped mass points connected with rigid rods and hinged together. The model is able to deform partially but cannot accurately model the flexibility as the rods are rigid. Furthermore fictitious forces are added between the different lumped masses [45].

6. **Multi-Body Model**: This model developed by Breukels [9] looks at using both spherical springs and linear springs to connect the different sections of the kite. The leading edge is taken to be stiff and fictitious stiffness parameters for the canopy are determined using experimental data. The model is very useful as it can model the flexibility of the kite properly however still uses fictitious stiffness forces. Furthermore the construction of the model is highly time consuming as it requires the determination of multiple parameters to define each block [9].

7. **Finite Element Model**: The finite element model further increases the complexity of the system. It involves having the kite divided using a mesh and the material parameters are used to define the kite's structural properties. It involves no fictitious forces and is accurate with modeling the flexibility of the kite. It has a high computational time and requires a detailed aerodynamic model. There are multiple difficulties in the meshing of the kite especially when combining the aerodynamic and structural mesh.

One can view the different structural models and their associated accuracy and computation time in Figure 2.1.

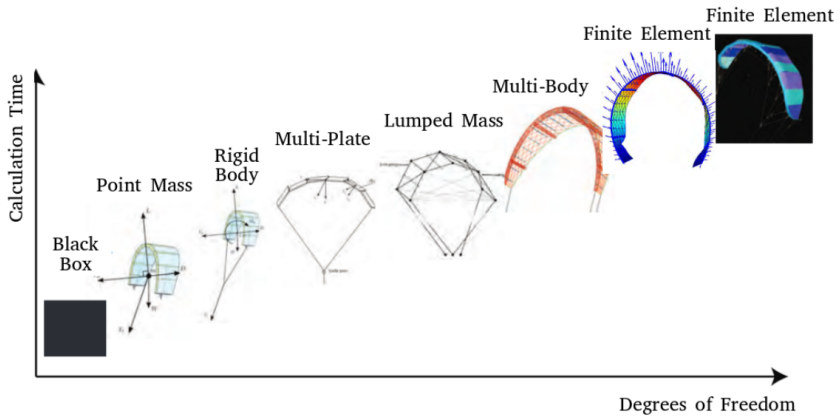

Figure 2.1: Structural models, accuracy vs computation time [15]

2.3. Aerodynamic Models

The usage of kites for power generation is a relatively new concept with limited research. Therefore much of the aerodynamic models and analysis relevant for LEI kites involves the combination of various natural systems including airplane and sails. Assessing the aerodynamics of LEI kites however poses multiple challenges arising due to flow separation, shape of the kite and its flexible nature. The different models used for the assessment of kites are explained below [15].

1. **Black Box model**: Like the black box structural model the aerodynamic model involves look up tables where the aerodynamic forces and moments are given as a function of the angle of attack. Furthermore correction terms are applied to account for gravity and turning. This model has been produced by Fetchner [16], where the model is also adapted to a four point model to allow control parameters. The model is accurate at predicting the performance of a kite and is also very fast however the models do require empirical data which limits its possibility as a designing tool.

2. **2D Finite Strip Model**: This model involves dividing the kite into multiple 2D sections as shown in 2.2a. The polars of the 2D section are determined using inviscid flow solvers such as XFoil at different angle of attacks. The 2D sections are then combined to form the 3D wing. When running the simulations with XFoil the 2D sections are assumed to be of infinite span and polars are calculated without 3D effects (cross-flow, lift induced drag, etc.) and deformation modes (jelly fishing, twisting, etc.). Another issue is that Xfoil and other 2D flow solvers are unable to accurately model separated flow and assess geometries with high Reynolds numbers [39].

3. **Breukels Aerodynamic Model**: Breukels aerodynamic model explained in reference [9] discretizes the 2D section in the chordwise direction as shown in Figure 2.2 thereby allowing the flexibility of the kite to be expressed. In order to determine the aerodynamic properties for the 2D section one can use the same approach as the 2D finite strip model. In the case of Breukels 2D CFD simulations were used to develop an understanding of the flow. This is then used to formulated the lift, drag and moment based on the airfoil thickness, camber and angle of attack. The sum of the force is known and the moment at the quarter chord point is known, one can use these constraints to determine the chordwise force distribution as shown in Figure 2.2b. This method is repeated for each 2D section. Estimates are made of the 3D effects using the Tornado VLM (Vortex Lattice Method) and are added to the solution.

   This method has received some feedback for improvement from Bosch [8]. He has criticised the formulation of the 2D polars, specifically regarding the linkage between the airfoil parameters and the polars. The spanwise velocity is ignored during the formulation and the 3D effect estimates at the end assume attached flow. Furthermore the method is inaccurate at predicting pressure distributions when there is separation (high angle of attack) and inaccurate when dealing with highly viscous flows (low angle of attacks) [8].

4. **Navier-Stokes Methods**: One can accurately model the flow behavior by resolving the incompressible Navier-Stokes equations. These equations allow one to describe the motion of fluids by ensuring that there is continuity and conservation of momentum. The continuity equation shown in equation 2.6 in tensor notation is used to express that the mass is conserved (divergence of velocity is zero). The momentum equation shown in equation 2.7 states that the momentum of the system is conserved. In the equation $\mathbf{U_i}$ represents the vector formation of the velocity (u, v, w) and $\mathbf{x_i}$ represents the directional vector (x, y, z), υ represents the kinematic viscosity and t is the time.

   By resolving the Navier-Stokes equations one is able to attain the flow behavior in the domain. The equations are however computationally expensive to resolve without simplifications. Therefore multiple theories are used to simplify the equations. The potential flow theory simplifies the flow by assuming it to be inviscid (frictionless) and irrotational (non-rotating fluid particles). This allows one to linearize the Navier-Stokes equations which can then be solved numerically using a combination of the lifting line theory (LLT) and vortex lattice method (VLM). In this method the wing is modelled using discrete vortices which at each time step in the simulation releases a vortices (with circulation representing the change in force). This vortex is a source and interacts with the bound vortices (used to represent the body) and other free stream vortices using Kelvin's theorem, i.e. conservation of circulation. One can then get a value for the bound vortex strength at each time step and thereby get the forces for each section at each time step. This technique is especially accurate for high Reynolds number and attached flow where the viscous layer is thin. For the case of LEI kites one cannot use this method due to the prevalence of separation, which is not accurately modeled using this method [8].

$$\frac{\partial U_i}{\partial x_i} = 0 \tag{2.6}$$

$$\frac{\partial U_i}{\partial t} + u_j \frac{\partial U_i}{\partial x_j} = \frac{-1}{\rho} \frac{\partial p}{\partial x_i} + \upsilon \frac{\partial^2 U_i}{\partial x_j \partial x_j} \tag{2.7}$$

   When resolving the Navier-Stokes equations a key challenge is accurately modelling the turbulence whilst limiting the computational cost. Three key turbulence modelling approaches exist namely, Reynolds Averaged Navier-Stokes (RANS), Large Eddy Simulation (LES) and Direct Numerical Simulation (DNS).

   DNS is the most accurate model as it resolves all temporal and spatial turbulent scales. In order to do this one requires a very fine grid and a small time step which leads it to be computationally expensive. One of the largest ever experiments using this method involved a Reynolds number of 4×10^4 to assess the flow properties inside a swirl burner. This analysis required a cell count of 2.6×10^9 [34]. Resolving a mesh size of this scale is not possible given the available resources.

When looking at the turbulence one can differentiate between the large eddies which are primarily due to the flows interaction with the body and the smaller eddies which are usually due to viscosity. The turbulence of the larger eddies generally have a stronger influence on the turbulent kinetic energy especially for flows with high Reynolds number. It is therefore highly important to have the large eddies modelled accurately [28]. The LES approach allows one to solve the large scale eddies explicitly and the small scale eddies implicitly. This involves separating key variables such as velocity, pressure etc. into a resolved part and a subgrid part. A variant of this is the Detached Eddy Simulation method. This hybrid method evaluates the region close to the wall using RANS and uses the LES method for other regions.

The RANS approach involves separating the flow into a time average part ($\overline{U_i}$) and the fluctuating part (U_i') as shown in equation 2.8 for the velocity. Using this and knowing that the mean of a fluctuating part is 0, one can simplify the Navier-Stokes continuity equation to equation 2.9 where the term $\rho\overline{U_i'U_j'}$ is the Reynolds stress term which is an unknown stress used to increase the diffusion of momentum similar to viscosity. This non-linear term can be modelled using different turbulence models. Out of the three models the RANS approach has the lowest computational requirement [5].

The computational cost associated with running a dynamic simulation whereby the turbulence scale variations can be visualized is beyond the scope of this thesis. It is therefore decided to use the RANS approach as it resolves all turbulence scales and the time averaging approach would be ideal for a steady state simulation.

$$U = \overline{U_i} + U_i' \tag{2.8}$$

$$\rho\Big(\frac{\partial\overline{U_i}}{\partial t} + \overline{U_j}\frac{\partial\overline{U_i}}{\partial x_j}\Big) = -\frac{\partial\overline{p}}{\partial x_i} + \frac{\partial}{\partial x_j}\Big(\mu\frac{\partial\overline{U_i}}{\partial x_j} - \rho\overline{U_i'U_j'}\Big) \tag{2.9}$$

For a CFD simulation the boundary conditions for a variable can be given using the Dirichlet boundary condition or the Neumann boundary condition. In the Dirichlet condition one specifies a fixed value of a parameter on the boundary, whereas in the Neumann boundary condition one specifies the normal derivative of a variable on a surface. The boundary conditions used for a flow simulation over an object is the pressure and velocity distribution on the far field boundary and on the object wall.

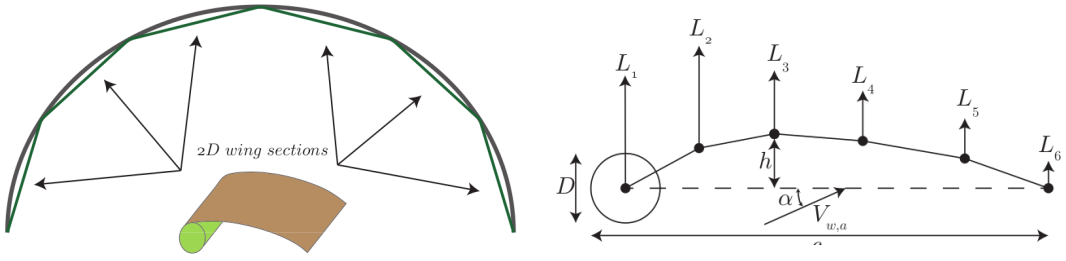

(a) Spanwise discretization

(b) Chordwise discretization

Figure 2.2: Breukels model sectional discretization [8]

2.3.1. Turbulence Modelling

The RANS approach has a term called the Reynolds stress term that has to be modelled. Key models include the $k-\epsilon$, $k-\omega$ and the variant $k-\omega$ SST. These models are better in different cases, and have different ways to represent the dissipation of turbulence, dissipation of energy and eddy viscosity.

1. $k-\epsilon$ model: This model includes two extra transport equations to represent the turbulence of the flow. It involves introducing two variables namely the turbulent kinetic energy (k) and the

turbulence dissipation (ϵ). It is accurate for cases with free shear wave flows, i.e. flows with small pressure gradients. For the kite it is expected that there will be high pressure gradients near the kite's surface, due to the thin canopy but low variations far field. The method involves resolving the Reynolds stress ($\tau_{t_{ij}}$) using equation 2.10 where S_{ij} is the mean velocity strain tensor, δ_{ij} is the Kronecker delta function and μ_t is the eddy viscosity. The eddy viscosity which represent the transfer of turbulent momentum is given by equation 2.11, where c_μ is a model coefficient which can be determined by equilibrium analysis and f_μ is a damping function [7].

$$\tau_{t_{ij}} = 2\mu_t(S_{ij} - \frac{\partial u_k}{\partial x_k}\delta_{ij}/3) - 2\rho k\delta_{ij}/3 \tag{2.10}$$

$$\mu_t = c_\mu f_\mu \rho k^2/\epsilon \tag{2.11}$$

2. $k-\omega$ model: This model involves convective transport equations for the turbulent kinetic energy (k) and specific dissipation rate (ω). This model unlike the $k-\epsilon$ function is more accurate in the viscous sublayer near the wall. One can define the Reynold stresses in the same way as the $k-\epsilon$ model using equation 2.10 but require a different function to resolve the eddy viscosity; given by equation 2.12, where ω is the specific rate of dissipation and k is the turbulent kinetic energy [7].

$$\mu_t = \rho k/\omega \tag{2.12}$$

3. $k-\omega$ SST model : This model combines the $k-\omega$ and $k-\epsilon$ models by using zonal model coefficients. This allows the model to use the $k-\omega$ model near the geometry and the $k-\epsilon$ model in free stream zones. The model also modifies the eddy viscosity by forcing the turbulent shear stress to be bounded inside the boundary layer. In order to apply the zonal model one has to firstly transform the $k-\epsilon$ formulation to that of $k-\omega$ and then to introduce two closure coefficients F_1 and F_2.

   F_1 has a value of 1 near the wall and a value of 0 far away so in order to attain the turbulence model constants ($[\sigma_k, \sigma_\omega, \beta, \gamma]$) denoted by Φ, one has to multiple the constants from the $k-\omega$ model by F_1 and the constants from the $k-\epsilon$ model by $(1-F_1)$ as shown in equation 2.14, where subscript 1 is used for the $k-\omega$ model and subscript 2 is used for the $k-\epsilon$ model.

   In terms of the eddy viscosity, the model includes the transport of turbulent stresses by modifying the eddy viscosity equation as shown in equation 2.13, where F_2 is a closure coefficient and Ω is the absolute viscosity.

   This model will be preferred as it is accurate for both the viscous sub-layer and also the free stream region. When implementing this model boundary condition for the turbulence kinetic energy (k) and the specific dissipation rate (ω) have to be introduced as initial conditions. For this thesis the turbulence kinetic energy for a normalized velocity is taken to be $1.5 \times 10^{-2} m^2/s^2$ for 2D cases and $3.1 \times 10^{-3} m^2/s^2$ for 3D cases. The specific dissipation rate is taken to be 1.224 $1/s$ for the 2D case and $2.37 \times 10^4 1/s$ for the 3D case.

$$\mu_t = \frac{\rho k/\omega}{max[1; \Omega F_2/(a_1\omega)]} \tag{2.13}$$

$$\Phi = F_1\Phi_1 + (1-F_1)\Phi_2 \tag{2.14}$$

2.3.2. Finite Volume Methods

The finite volume method (FVM) involves discretizing a continuous system of differential equation. One can then resolve the equations for the discrete points in the domain. It is based on the principle that volume integrals can be expressed by surface integrals. One can see this for the 1D case in Figure 2.3 where the system is divided into multiple control volumes. For each control volume the variables are computed (in the center of the cell) and then interpolated to the cell surface.

The interpolation scheme selection is based on five criterions namely: conservativeness, boundedness, transportiveness, accuracy and computation time. Conservativeness states that the interpolation scheme should give the same value of flux at the face of adjacent volumes, when using FVM this criteria is enforced (not the case for finite element methods). Boundedness states that the value at each node should converge. Transportiveness assesses the ability of the interpolation scheme to address diffusion and convection in the interpolation process, this criteria is judged by the Peclet number. In order to calculate this variable one can use equation 2.15, where Sc_t is the turbulent Schmidt number and Re_L is the Reynolds number. For low Peclet numbers a cell evenly influences the neighbouring cells (like a source), but for high Peclet numbers the flow is dominated by convection. For cases dominated by convection, central differencing (which involves taking the average of the two neighboring nodes to compute the value of the variable at the surface) is inaccurate as it gives equal priority to upsteam and downstream flows. Instead in such a case upwind differencing or power law schemes should be used. For this study a Reynold's number of 6×10^6 will be used, as the Peclet number is proportional to the Reynolds number, one can expect the value of this parameter to be large. The simulation setting will therefore use upwind interpolation. The simplest scheme with this setting uses the 1^{st} order differencing scheme where it takes the value at the connecting surface to be the value at the node upwind. One can improve the accuracy by selecting a higher order scheme such as QUICK, whereby the parameters are interpolated by looking at the variation of the parameters from a location further downwind. Using such schemes however negatively impact the computational cost, due to the limited resources available for this study the 1^{st} order scheme is deemed sufficient.

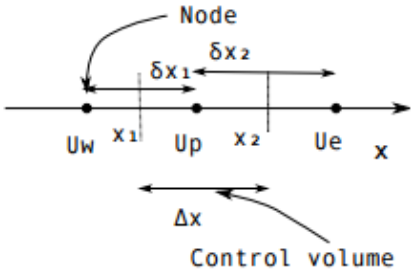

Figure 2.3: FVM discretization [13]

$$Pe = \frac{LU}{D} = Re_L \cdot Sc_t \tag{2.15}$$

2.4. Fluid-Structure Interaction

Modelling of kites is very difficult due to the high flexibility and thus high coupling of the aerodynamics and structure. A good dynamic model looks at having high accuracy whilst still being low on computation time. This section will cover the monolithic and the partitioned method of combining the fluid forces with the structural model. Furthermore it will discuss mesh morphing and the various challenges associated. Also the current stage of fluid-structure interaction (FSI) models and how the thesis study will contribute to kite modelling will be presented.

There are two broad categories one can use for the FSI problem namely, monolithic and partitioned methods as shown in 2.4. In a monolithic method the interaction between the structure and fluid are treated synchronously. By doing this one is able to eliminate errors incurred by asynchronity and use the conservation properties at the interference. This allows one to ensure stability and use a large time step [32].

Partitioned solvers on the other hand separate the structural solver and the aerodynamic solver and solve each at different time steps [33]. Typical sequencing of such a system can be summarized in 5 steps [33]:

1. Transfer the motion of the structural boundary to the fluid.

2. Update position of moving fluid mesh.

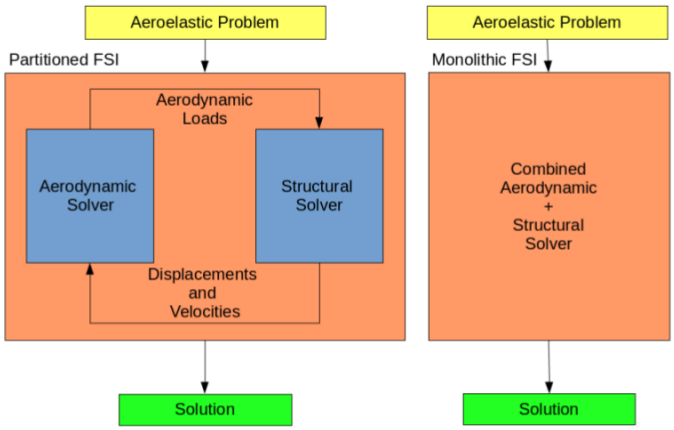

Figure 2.4: Partitioned vs Monolithic FSI solvers [15]

3. Advance fluid system in time and run fluid simulation and obtain pressure.

4. Transfer aerodynamic pressure to structural model and obtain load.

5. Advance Structural system in time due to loads.

In this process one has to transfer the forces to the structural model and update the motion in the aerodynamic model. The surface meshes at the FSI interference may or may not match. Latter requires mapping from one mesh to the other. The aerodynamic mesh is the one that is generally adapted, as the structural meshes are generally more coarse and when modifying a meshes, one either loses accuracy in the pressure fields or significantly increases the computation time of the structural analysis [33].

The partitioned method also involves a time lag between the aerodynamic and structural solution and will lead to inaccuracies in energy conservation causing the system to be unstable. This side effect leads to there being restrictions on the admissible time step. One can limit this error by improving the coupling between the two systems. This is achieved by repeating within each time step alternate fluid and structure solutions until convergence [32]. One can further use prediction techniques where the algorithm uses previous iterations/time steps to make an educated guess for the next iteration [33]. One can view the influence of the prediction method in Figure 2.5.

Partitioned methods whilst less accurate offer four key advantages over monolithic methods namely customizability, independent modelling, software reuse and modularity [17]. The advantage of modularity and software reuse is especially relevant for research institutions as it allows independent research work to be combined and there to be flexibility in terms of selecting a model. TU Delft has adopted the partitioned solver approach for its FSI environment, as discussed by Breukels in [9] and Bosch in [8]. In both these cases the mesh for the structural analysis is coarser than the one for the aerodynamic model and weighting factors are used to convert the CFD discrete values to a coarser distribution such that the loads aligns with the structural model. Bosch however does add a prediction module for the structural module that uses Newton-Raphson method to reduce asynchronous errors and allow iteration of the solution at the next time step. This also significantly reduces the computation time for the structural analysis.

Currently, there are efforts by TU Delft to further develop the FSI environment used by TU Delft. This thesis aims to help in the development of the aerodynamic module using CFD. Currently, CFD analysis has been performed by Deaves [15] for the V2 kite at different angles of attack. Limited information is available regarding how the pressure distribution changes for a deformed kite when turning. This thesis will explore this by performing CFD simulations for a turning kite. The approach will use a RANS simulation with a $k-\omega$ SST turbulence model.

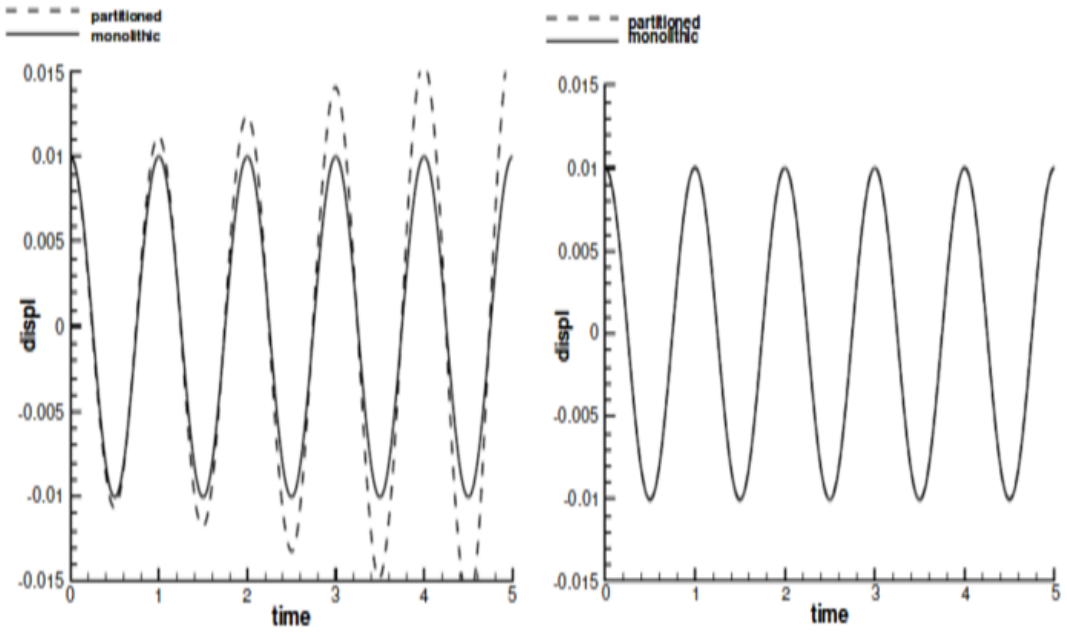

(a) Without prediction techniques (b) With prediction techniques

Figure 2.5: Partitioned vs. monolithic results for an oscillatory piston movement [33]

2.5. 3D Kite Analysis

This chapter has looked at the key challenges associated with kite modelling. It has been shown that one has to make a trade-off on accuracy vs the computation time. While it would be ideal to have a detailed FEM model for the structural analysis, it requires material and structural properties for each element and has a high computational cost. The same can be said for the aerodynamic analysis, while the DNS approach does allow the user to take into consideration all temporal and spatial turbulent scales required for an accurate aerodynamic analysis. The associated computational cost is excessive. Achieving the goal of having an accurate 3D flow analysis incorporated with an accurate structural basis, in an FSI environment therefore poses a significant challenge.

A potential approach could be to use a low computational cost model with results incorporated from an accurate methodology. An example for this would be to have the results from a high fidelity CFD analysis incorporated with a 2D finite strip model. One can thereby have local polars for a specific case that have taken into account key 3D flow effects. This is the approach used by Breukels and Bosch in their models, wherein the results from 2D CFD computations with the VLM is incorporated with the 2D finite strip model.

This thesis will provide a basis to improve the aerodynamic parameters by performing perform 3D CFD computations to attain aerodynamic parameters. An approach will be set up whereby a kite with be simulated using the RANS approach with a $k-\omega SST$ turbulence model and local aerodynamic polars will be extracted. The study will look at understanding how the flow behavior develops at different sections along the kite for two cases namely, normal operation and a case with turning-induced shape deformation. Key deficiencies of this method when performing 2D CFD simulations will be understood and attempts will be made to relate the 2D sectional simulations to 3D sectional data, thereby quantifying the influence of 3D flow effects.

The thesis will firstly discuss the methodology used to maximize accuracy whilst limiting computational cost with the RANS approach. It will discuss a 2D sectional study similar to that of the kite, that will be used for validation of the method. The 2D study will then be compared with results of 3D sectional studies to understand the influence of 3D flow effects. Additionally the influence of turning induced shape deformations will be understood, both on global aerodynamic parameters and sectional polars.

3

Methodology

This section will cover the methodology used in the setup of the simulation model. It will cover the goals of the meshing process, the simulation settings used for the setup and will address the setup for turning-induced deformations. The section will also perform a study to assess the quality of the mesh, by performing a trade-off on key boundary layer mesh parameters and computational cost.

3.1. 3D Meshing

As mentioned in section 2.3.2 in order to solve the Navier-Stokes equations within a system it is required that the system be discretized into small sections where the governing equations are resolved. This is achieved by meshing the flow domain. There are three key aspects one has to keep in mind when meshing, the first is to limit the kite's geometry alterations such that key flow behavior is properly recreated. The second involves ensuring that the quality of the mesh is high such that the results are accurate and computational cost is minimized. The third objective is to have limited amount of cells in the domain such that the computation time is reasonable whilst still properly addressing flow behavior.

The mesh can be defined as either structured or unstructured. A structured mesh involves representing a mesh with regular connectivity. This is achieved using quadrilateral (2D) or hexahedral (3d) shapes only. An unstructured mesh involves irregular connectivity within the mesh and has no restrictions on cell shape. One can view the difference in Figure 3.1. Structured grids generally offer advantages in terms of solution efficiency and quality. Unstructured grids are useful for discretizing complex domains, which would not be possible with structured grids however they do negatively effect the computation time, [21]. It would be better to use the structured grid approach however due to the high curvature of LEI kites, the structured approach will cause cells far field to squeeze. An approach that is conventionally used is to have a structured grid (which is very fine) near the geometry and have an unstructured grid farfield. This way the viscous sublayer can be efficiently resolved with the structured layer and the flow farfield can be resolved using an unstructured grid. The meshing process can thereby be divided into three major sections, the surface meshing of the geometry and far field boundary, the boundary layer over the kite and the unstructured grid between the boundary layer and far field boundary.

In order to generate the mesh it is possible to use either a body fitted grid or a cartesian grid. Body fitting grids evaluate the geometry inside the domain and creates a mesh based on the surface mesh of the geometry. One has high control on the growth of the cell size within the domain. It however is highly sensitive to sharp changes in cell sizes which is a critical aspect with the kite considering the thin trailing edge. The Cartesian grid approach on the other hand refines all cells in the domain and removes cells which fall inside the boundary of the kite. Refinement is done incrementally by cutting cells a number of times till the required refinement levels are reached. This approach however leads to innacurate representation of the body as the cells might cut through the body of the kite [11]. In this study a combination of the two will be used. Cartesian grid will be used in the domain for refinement purposes and in order to ensure the body is accurately modelled, the cells that intersect with the body will be snapped to align with the body. This approach is possible with the module cartesianMesh with the tool cfMesh.

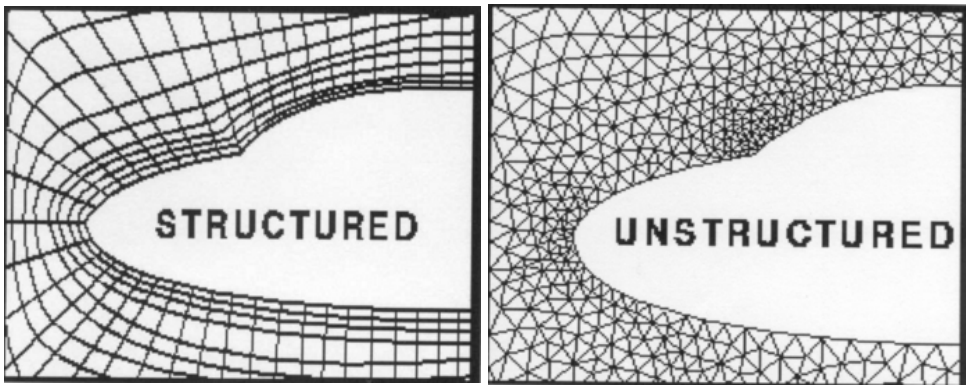

Figure 3.1: Structured vs. unstructured mesh [21]

3.1.1. Surface Meshing

The surface meshing process involves meshing the surface for both the kite and the far field boundary. It involves firstly, simplifying the geometry by defeaturing and generating the far field boundary for the analysis. Surfaces can be defined in one of two ways either using a set of conforming patches or in a discrete manner (e.g. surface triangulation). The goal of surface meshing is to efficiently represent the body with limited finite elements so as to reduce the computation time whilst also limiting the defeaturing of the kite to achieve accurate result.

The initial geometry provided using SurfPlan is considered to be an accurate representation of the kite. The geometry however poses some challenges. Firstly, the canopy is modelled as an infinitely thin surface, this poses challenges with the considered meshing tools as they require a closed geometry; a thickness of 2mm is provided to resolve this. Secondly, the kite has sharp edges when connecting the canopy with the leading edge and at the connection points of the struts. Resolving these sharp edges and creating a boundary layer is extremely complicated and would require many cells so these regions will be smoothened. Lastly, as the struts are present on the underside of the canopy the aerodynamic influence that they will have is assumed to be negligible. Furthermore due to the curved shape and complexity regarding the attachment points the associated computational cost is very high. It is therefor decided to remove the struts for the CFD analysis. Similar alterations were also made by Deaves [15] in his analysis along with adaptions to the tip of the kite. One can see the 3D adaptions made my Deaves in Figure 3.2a, similarly the 3D alterations made in the current model can be seen in Figure 3.2b. One can see that although both have curved out the kite, the tip is more accurate with the new approach. This is essential as the thesis focuses on the influence of turning deformations, which are initiated at the tip section. One can also see the 2D sectional differences in Figure 3.3 as can be seen the newly adapted cross-section better resembles the cross-section of the original geometry, and would offer more accurate flow behavior. In order to validate these geometry alteration a 2D validation study has been conducted in section 4.1 which compares the kites sectional 2D geometry with a cross-section that resembles the kite.

In order to limit the cell count (and thereby the computational cost) used to represent this geometry one can divide the geometry into patches that represent key geometric attributes of the kite. One can then refine each patch separately such that the geometry is properly represented. In the case of the kite, one can use coarse cells to represent the canopy as the shape has a limited curvature, but have refined cells for the leading edge and trailing edge such that the geometry is not defeatured.

In order to assess the surface mesh one can look at surface distortions in the mesh. Distortions can be characterized by two parameter; level of skewness and stretching (angle deformation, area deformation). For aerodynamic purposes area distortions significantly impact the shape of the body which can be viewed as artificial roughness and will significantly impact the outcome of a simulation, and skewness will effect computation time and mesh quality. In order to minimize the skewness one can use criteria's such as Delaunay sweep, in this method a circle is constructed out of the mesh points of a triangle and no vertex is allowed inside the circumference of the circle [19] [46].

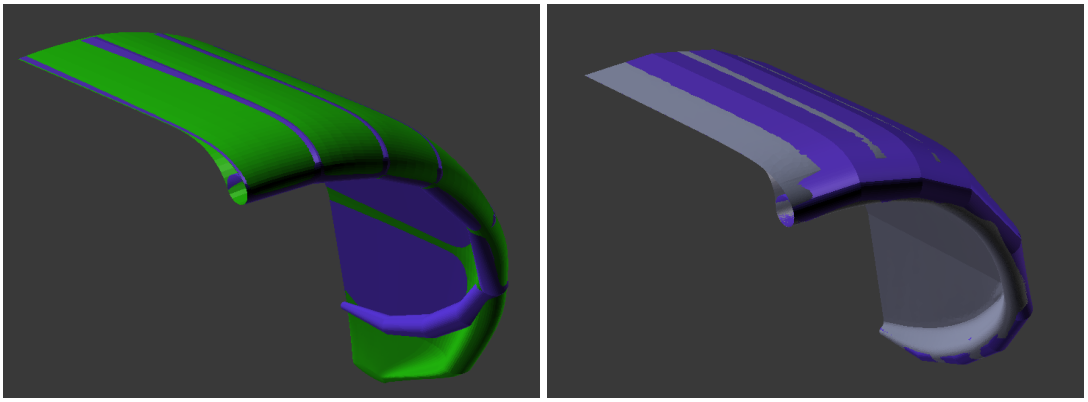

(a) Variation between original geometry (blue) and Deaves geometry (green) [15]

(b) Variation between original geometry (blue) and created geometry (grey)

Figure 3.2: Defeaturing of geometry

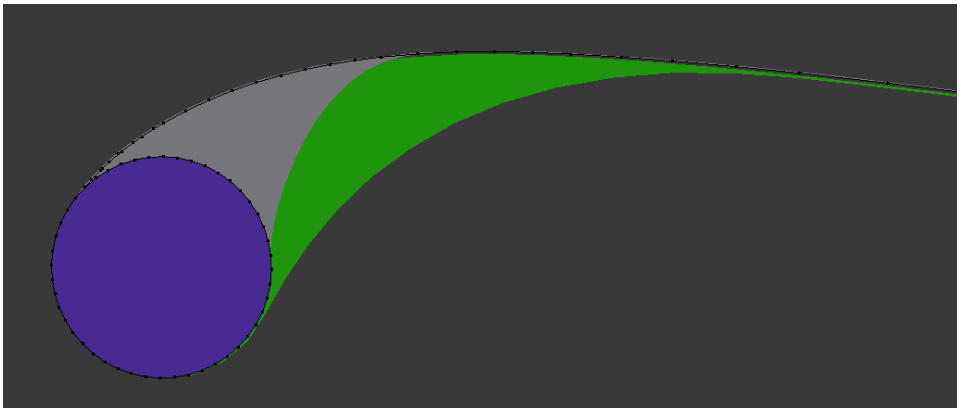

Figure 3.3: 2D cross-sectional variations between original (blue), Deaves (green) and newly adapted (grey) [15]

3.1.2. Boundary Layer

A boundary layer mesh is required to resolve the viscous sub-layer close to the geometry. For high Reynolds number the boundary layer is thin [44], requiring the velocity to accelerate from 0 at the boundary to the freestream velocity. One can therefore expect there to be steep velocity gradients in this region. In order to accurately model this one would require a fine mesh in wall normal direction. The velocity gradients spanwise and streamwise however do not vary significantly therefore one may use cells with high aspect ratio.

For the kite geometry one can expect that on the suction side (above the canopy) the flow will be attached and there will be adverse pressure gradients. However for the pressure side (below the canopy), the cylinder will act as a bluff body. One can therefore expect boundary layer separation (fluid flow detaches from geometry) and very strong flow oscillations in the cylinder's wake [52]. The length of this wake is difficult to assess due to the presence of a curved canopy but one may see flow attachment near the tip. With flow oscillations and high turbulence there would also be significant velocity gradients in both the spanwise and streamwise direction. Ideally one should therefore have a boundary layer imposed on the suction side and near the tip of the pressure side of the geometry. Whilst it was possible to create an adaptive boundary layer, the cartesian approach of mesh refinement lead to coarser cells (cfMesh tool creates the boundary layer by dividing the last cell) which would be worse in modelling the turbulent behavior. This style of mesh was used when performing the mesh validation study in section 3.2, where the goal was to assess the impact of boundary layer parameters on results. One can classify these boundary layer parameters by, the boundary layer mesh shape, first cell height, the stretching ratio between the layers and the number of layers.

One can have either a single-block grid or a multi-block grid. In a single-block grid, a mesh block

is refined in a single structured approach to conform to the shape of the geometry. This distortion can be classified in three ways, O-grid, C-grid and H-grid. In an O-grid scheme oval shaped loops where the last point wraps around and meets the first point. In the C-grid scheme C shaped loops are used, where the lines will point gradually reduce the curvature to have points in the same direction. One can see the difference in Figure 3.4. An H-grid represents any shape that does not fall in the previous categories. Luton conducted a study on the NACA 0012 using these two methods in reference [27]. Both showed very good results in the transonic case. It was identified that the O-grid was better at estimating the pressure coefficient in the vicinity of the leading edge and flow gradients at the trailing edge; however the C-grid is able to align points in the direction of the wake, which improves the wake resolution [27]. The multi-block grid approach used by tools such as blockMesh have the option of dividing the domain into multiple blocks allowing for flexibility in selecting the grid type.

The first cell height is characterized by a non-dimensional parameter, y^+ value. It's value has to be varied depending on the flow characteristics and detail of accuracy required as shown in Figure 3.5. For regions where there is attached flow and high viscous behavior one should use a low y^+ value whereas for regions with turbulent flow the y^+ required can be higher and still properly address the flow behavior. In the case of kites, the attached flow regions have high velocity and pressure gradients therefore wall functions cannot be used and the laminar sublayer must be resolved. One must therefore use a y^+ value that falls in the low bracket and in the order of $\mathcal{O} = 1$ [25]. One can relate this parameter to the desired cell height by equation 3.1 where u^τ is the friction velocity and υ is the kinematic viscosity. The friction velocity is used to characterize the turbulence strength and laminar sublayer thickness and is calculated using equation 3.2 where τ_w is the wall shear stress. The wall shear stress can be calculated by relating to the skin friction coefficient (C_f) with equation 3.3, in this equation the 1/7 power law approximation with experimental calibration over a flat plate is used to relate the Reynolds number to the skin friction coefficient. One can thereby estimate the required height of the first layer to be approximately $1 \times 10{-}5$ m for a y^+ of one using equation 3.4. The y^+ value is dependent on the wall shear stress which valies on the kite, one should therefore iterate the height such that the $y^+ < 1$. This layer height however posed multiple challenges associated with mesh quality so the cell height is adapted to 2×10^{-5} m.

The boundary layer height (Δ) and growth factor are the other two parameters of significant importance. A growth factor has to be selected that allows for minimal computation time while still capturing the boundary layer properties. Spalart [47] recommended to select a value lower than 1.4 and approximately equal to 1.25 to accurately capture the log layer. As capturing the boundary layer near the kite accurately is of prime importance for accurate pressure and force computations, a value of 1.2 is selected. For the boundary layer height an iterative process is recommended; where one tries to attain a height that covers a majority of the boundary layer whilst ensuring that the boundary layer shape does not converge. In order to do this one would ideally use an iterative approach in selecting a height until the velocity at the last layer is approximately 99% of the free stream velocity. For an initial guess of the height one can use Schlichting equation for turbulent boundary layers height over a flat plate shown by equation 3.5 [44], which leads to a boundary layer height of approximately 0.045m. This however poses challenges with mesh quality so an initial height of 9×10^{-3} m is selected.

The impact of the parameters used in the boundary layer definition highly influences the accuracy of flow separation and thereby the resulting flow characteristics and behavior. Furthermore due to the significantly thin sub-layers it has the majority of mesh cells. The impact of varying key parameters in the boundary layer on the accuracy has therefore been conducted in section 3.2.

$$y^+ = \frac{u^\tau y}{\nu} \tag{3.1}$$

$$u^\tau = \sqrt{\frac{\tau_w}{\rho}} \tag{3.2}$$

$$C_f = \frac{\tau_w}{0.5\rho U_\infty^2} = 0.0592 Re_x^{-1/5} \tag{3.3}$$

$$y = \frac{y^+ \nu}{\sqrt{0.0296 U_\infty^2 Re_x^{-1/5}}} \tag{3.4}$$

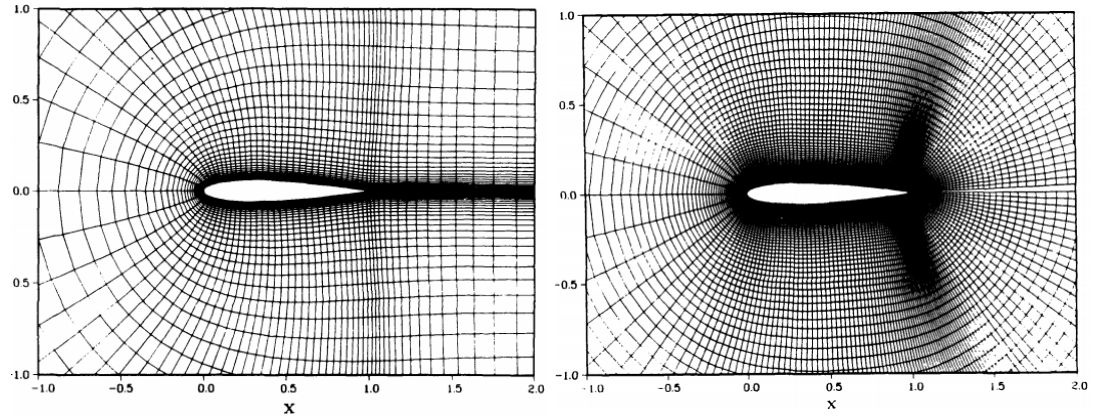

(a) C-grid

(b) O-grid

Figure 3.4: C-grid vs O-grid for Naca 0012 [27]

$$\Delta = \frac{0.37x}{Re_x^{0.2}} \tag{3.5}$$

3.1.3. Unstructured Mesh

In order to simulate the complete flow behavior of the kite it is important to have a mesh that covers the whole system, i.e. until a farfield point where the flow interference from the kite is negligible. As one moves away from the kite its influence on the flow field is incrementally reduced. One can therefore adapt the mesh such that as one moves further away from the kite the size of the mesh size increases incrementally; thereby limiting the number of cells and computational cost. The resultant impact of the domain size on the number of cells is therefore very limited. Selecting a criteria for the domain size, for which the accuracy errors are considered acceptable is upto the user. It has been identified by Deaves that by using 60 semi-span chords the accuracy levels are acceptable; only 0.2% difference in lift coefficient from using 80 semi span chords [15], this can be a basis for this assessment.

Structured meshes are the most sought after technique for meshing a system as it is computationally efficient, has easily define normals and is able to align with the flow [12]. Unfortunately, this approach has not been investigated in this thesis, due to limitations of the tools considered. The hybrid approach is considered sufficient for most aerodynamic studies. In this approach a structured mesh is used for the boundary layer and an unstructured grid is used for filling the domain. For an unstructured grid there are many possibilities for mesh shapes e.g. tetrahedrals, polyherals, pyramids etc. The most prevalent shape is that of a tetradral and can be generated automatically in most tools due to their simple shape and planar faces (ease in determining the centroids). However it struggles to align with the flow and would require more cells to fill the domain as it has fewer faces. Mesh quality is a serious concern with the kite due to its high curvature and thin trailing edge, leading to significant variations in size for adjacent cells.

Cell skewness is a factor used to quantify the stretching factor of a mesh element. The cell skewness is the ratio between the distance between two adjoining cell centres and the distance between their intersection with their common face and the centre of that face. For the two quadrilaterals in Figure 3.6a, the skewness is given by $\frac{mag(x)}{mag(\delta)}$. Non-orthogonality is another quality issue that tetrahedrals face where two adjacent cells centers do not form a perpendicular line with the cell face as shown in Figure 3.6b. The quality issues have also been identified by Deaves for LEI kites at the leading and trailing edge of the kite when transitioning from the structured boundary layer [15]. This issue was resolved with the use of multiple non-orthogonal correctors, which unfortunately did negatively impact the computation time required for the simulation. The use of polyhedrals is a relatively new technique and aims to resolve the lapses of tetrahedrals. It basically involves combining multiple tetrahedrals to form a larger shape. It has significantly more faces (more than 4) leading to faster convergence and better determination of cell gradients. It is also better at resolving the quality issues mentioned

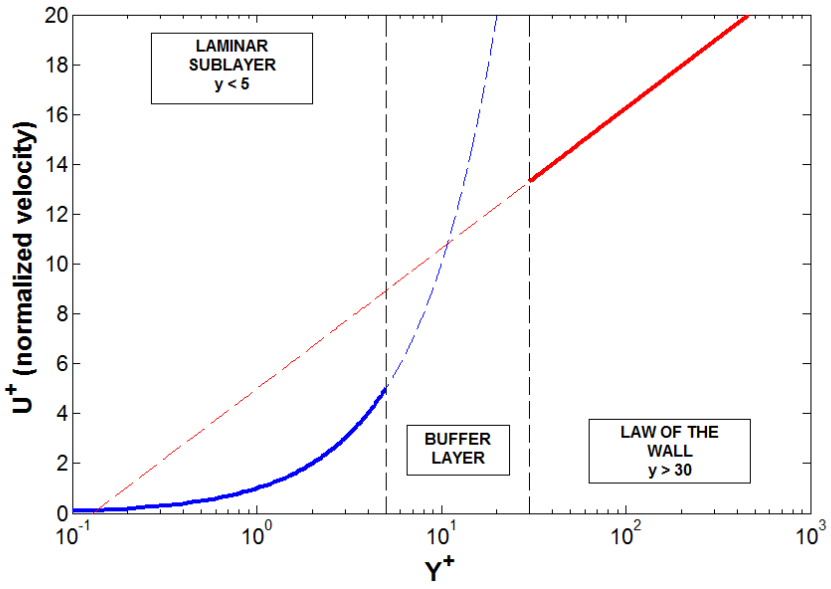

Figure 3.5: Required y^+ resolution [25]

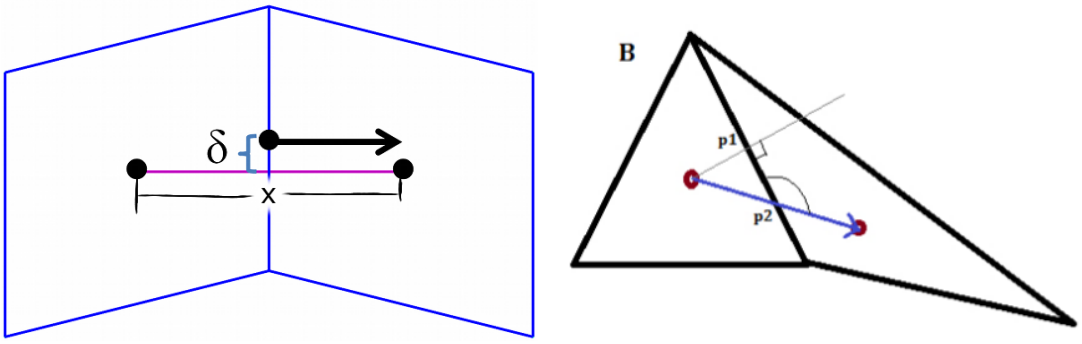

(a) Cell skewness [41]

(b) Non-orthogonal mesh angle [15]

Figure 3.6: Quality issues with tetrahedrals

(skewness and orthogonality). Polyhedral mesh also consume lesser RAM and have a lower mesh generation time. It however is a very complicated shape and requires many adjacency relations for each boundary cell (which could slow the simulation). It also could face quality issues if the polyhedrals faces are not planar and there is possibility of convex angles [6]. It is believed that by using polyhedral meshes computation time could be reduced as convergence will be acheived in fewer iterations.

An initial mesh is generated using the approach and while the quality of the mesh is improved in terms of non-ortogonality and skewness when compared with Deaves work [15]. The quality of the mesh is still quite low and requires additional work. The non-orthogonality has been limited to 76 degrees and skewness to 2.7. One can therefore perform the simulation with one less non-orthogonal corrector, which should significantly improve computational time of each time step and also lead to faster convergence.

3.2. Influence of Mesh Parameters

Once the initial mesh has been generated it is important to ensure that the influence of mesh parameters on the accuracy of the results is limited. This is achieved by varying key parameters in the mesh and checking the influence this has on the results. The accuracy of the results is largely governed by the flow behavior near the kite. The focus of the study will therefore be largely associated with the

boundary layer parameters. As mentioned in subsection 3.1.2 the boundary layer mesh is required on the suction side to capture the high velocity gradients near the surface. In this study the impact of variations in y^+ value and boundary layer height on the suction side will be assessed. It is believed that by reducing the y^+ value the flow separation behavior will be more accurate. Whereas by increasing the boundary layer height the flow development of the viscous layer will be improved leading to a better transition to the unstructured mesh. This will lead to significant improvements in the accuracy and convergence of the solution. An initial boundary layer with first cell height of $2 \times 10^{-5} m$ and a boundary layer height of 0.009m shown in Figure 3.7 will be used as a base case for comparison. The comparison will be run at an angle of attack of 27.5 degrees. One can see the impact of the different parameters on the results in Table 3.1. From the results it can be seen that the boundary layer height has significant impact on the overall results of the simulation, while the results do not vary significantly when the initial cell height is changed. The optimization will therefore look at increasing the boundary layer height to 1.4×10^{-2}. The impact this mesh adaption has on the results can be seen in section 4.2.

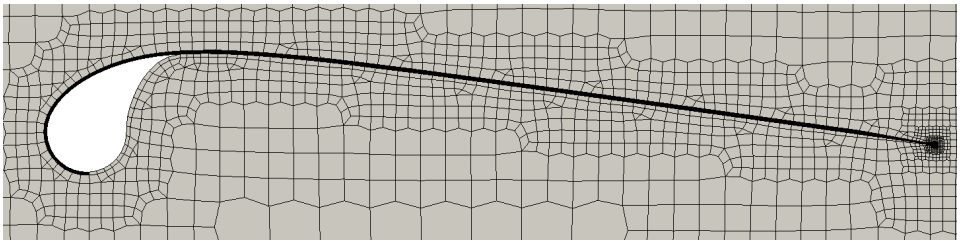

Figure 3.7: Initial boundary layer for optimization

Table 3.1: Impact of boundary layer parameters on results

First Cell Height (m)	Boundary Layer Height (m)	Cl Variation (%)	Cd Variation (%)	Change in Number of Cells (%)
2×10^{-5}	9.4×10^{-3}	-	-	-
1×10^{-5}	8.2×10^{-3}	-0.413	0.528	8.70
5×10^{-6}	8.5×10^{-3}	-0.311	0.519	20.3
2×10^{-5}	1.4×10^{-2}	-0.329	0.973	5.95
2×10^{-5}	2×10^{-2}	-1.01	1.27	11.8

3.3. Turning Kite Deformations

In order to model the deformations associated with the turning of the kite one can use the developed by Verheul using the tool Abaqus. This model uses an explicit finite element model and is linear elastic, requiring the Poison ratio and Young modulus for each element. For the canopy the direction of the fibers are assumed to be at 45 degrees, thereby having isotropic behavior. The bridle is modelled by using multiple spring damper systems to represent the flexibility of the lines. The model uses Breukels aerodynamic model, where the local sectional properties are used to generate kite polars, which are subsequently discretized along the chord [9] [51]. The Abaqus simulation is run at an angle of attack of 10 degrees by decreasing the length of the right steering line by 0.5m and increasing the length of the left steering line by 0.5m. This deformation would result in a rightward turn. One can see the resultant deformation in Figure 3.8, as can be seen the deformation involves a reduction in curvature on the right side (side with control input) and a pull towards downwards towards the KCU. Furthermore due to a reduction in bridle forces on the left there is a lack of structural rigidity leading to an increase in curvature. There are some accuracy issues identified in the model. Firstly the model is unable to represent pulleys present in the bridle system which results in slacking of the bridle lines and a stronger twist on the leading edge. Whilst adding pulleys in the overall model might not be possible it would be possible to adapt the length of the bridle lines when initiating the simulation to account for the changes in bridle lengths.

The kite geometry is recreated using Blender. Blender is a computer graphics software that can

be used to create 3D models. This tool has fuctionalities where it can recreate deformations. Due to the prevelance of strong local deformations it was not possible to use a simple twisting or bending deformation to recreate the model. Instead, the approach used involves a combination of castings and warps to fit the model, the resultant model compared to the Abaqus geometry can be seen in Figure 3.9. As can be seen there are some features such as the local buckling of the canopy and the sharp twist at the tip of the kite which is not accurately modelled with the blender tool. The focus of this study is to understand the influence of these deformations on the aerodynamic performance when turning. The accuracy of the model would however require improvements when considering optimization of turning performance.

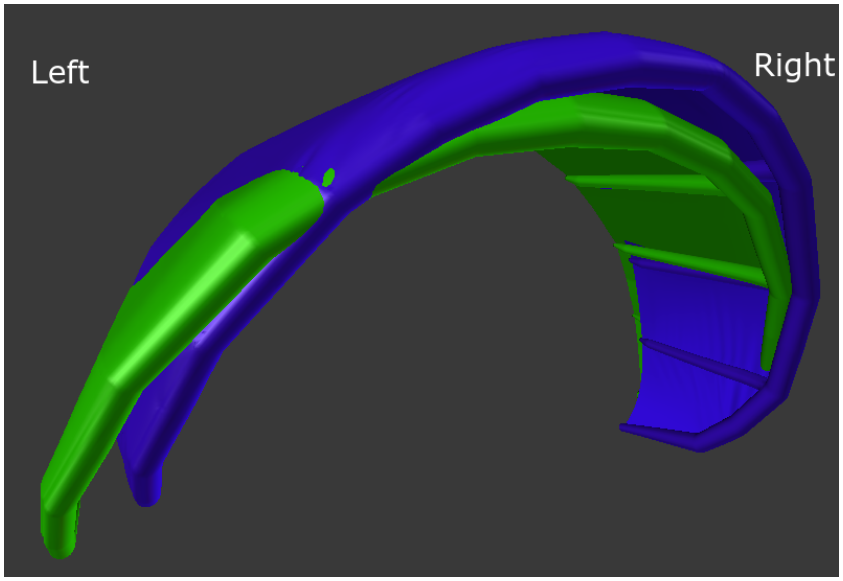

Figure 3.8: Undeformed Kite Model (green) Compared with Deformed Kite Model (blue)

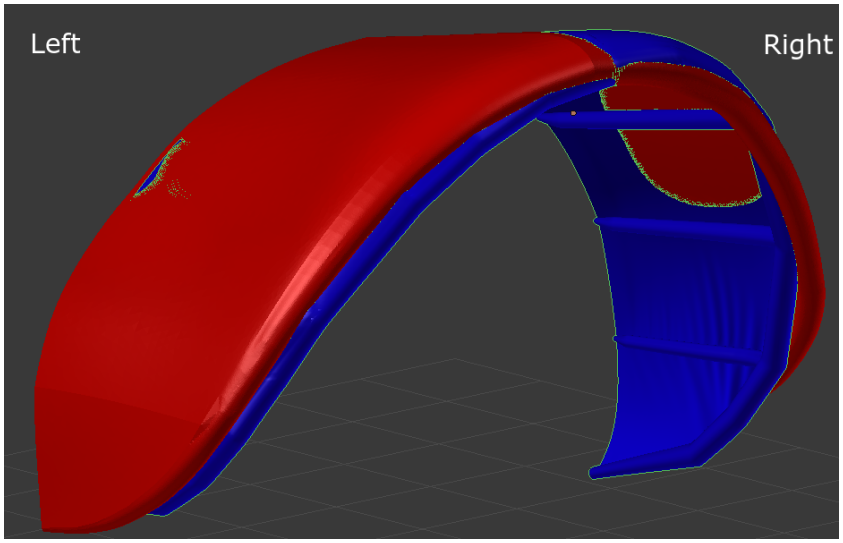

Figure 3.9: Model generated with blender deformations (red) compared with model provided by Abaqus (blue)

When generating the mesh it is important to note that the kite model is not symmetric. While for the normal case the use of a symmetric boundary condition can be used to divide the kite in the mid span section, this is not possible for the deformed kite. One therefore has to mesh the whole kite when performing the analysis. Furthermore when the kite is turning as shown in Figure 1.7 the wind is not perpendicular to the kite but has a varying slip angle. While at the start of the deformation the slip angle can be considered to be zero during the turn the angle varies depending on the turn radius. For

this analysis the goal will be to understand the impact of the deformations locally and globally at the initial stage of the turn. It will therefore be limited to flow with no slip angle.

3.4. 3D Simulation Setup

There are multiple tools available for the simulation of the kite, in this thesis the open source tool OpenFOAM will be used. This software based on C++ has a collection of solvers and utilities and can handle a large variety of CFD cases, including incompressible fluid flow. One can use either a steady or a transient solver for the simulation. Transient solvers allow for time based simulations thereby including dynamic effects of the flow. This approach however does lead to a substantial increase in the computation time. Due to time constraints, a steady state solver to assess the aerodynamics of the kite should be sufficient for this study. SimpleFOAM is the steady-state solver for incompressible fluids in OpenFOAM and one can use it to solve the RANS equations.

Solving the Navier-Stokes equations to attain the flow properties (velocity, pressure) poses a challenge as the pressure cannot be expressed explicitly. The SIMPLE algorith uses the Semi-Implicit Method for Pressure Linked Equations to resolve this issue. This process involves having an initial estimate of the pressure, resolving the continuity equations and correcting the pressure until the solution converges. One can summarize the algorithm as follows [38]:

1. Set the boundary conditions
2. Solve the discretized momentum equation to compute the intermediate velocity field
3. Compute the mass fluxes at the cells faces
4. Solve the pressure equation and apply under-relaxation
5. Correct the mass fluxes at the cell faces
6. Correct the velocities on the basis of the new pressure field
7. Update the boundary conditions
8. Repeat till convergence

An additional option of ”Consistent” is available in OpenFOAM which modifies the momentum equations such that there is no need for under relaxation in the pressure equations. This results in a faster convergence [37]. A detailed description of the solution parameters and finite volume schemes can be seen in Table 3.2. These schemes have been selected based on the recommendation of Joel Guerrero [20].

Table 3.2: OpenFOAM Simulation Parameters

Finite Volume Schemes		**Solution Parameters**	
Gradient	cellLimited leastSquares 1.0	Matrix Solver (P)	PCG
Laplacian	Gauss Linear Limited 0.5	Matrix Solver (U, k, ω)	PBiCG
Divergence (U)	bounded Gauss linearUpwind grad (U)	Relaxation Factor (U, k, ω)	0.9
Divergence(k, ω , ϕ)	bounded Gauss upwind	Tolerance (p,U,k)	10^{-08}
		nNonOrthogonalCorrectors	3

4

Results

In this section the simulation results for 2D splitter plate and 3D kite will be presented and analyzed. The chapter will be divided into three sections. The first will present the results of a 2D splitter plate study. This will provide insight into the selected method's capabilities to assess the flow around the kite. The second section will then present the results for both a non-deformed and a deformed kite. The results presented will include both sectional as well as global aerodynamic parameters. The last section will cover the precision of the results and will address the convergence criteria's set for the solution.

4.1. 2D Splitter Plate Study

In order to validate the usage of this method to assess the flow behavior around the kite, a 2D case similar to the sectional shape of the kite will be simulated. The study will refer to an unpublished study by NASA [29], which looks into the effect of leading edge booms on two-lobed parawings. The 2D shape of the sections considered (splitter plate) is shown in Figure 4.1 and has similarities with the shape of the kite, due to its circular leading edge and tangential connection with the canopy as shown in Figure 4.13. Due to these geometrical similarities it is hypothesized that there will be similarities in flow separation on the pressure side. The flow on the suction side is expect to be different due to the curvature of the canopy near the leading edge.

The goal of this study is to evaluate the validity of the approach mentioned in section 3. Due to the similarities in geometry mentioned, if this approach is able to accurately model the aerodynamics of the 2D splitter plate one would have greater confidence of this method in modelling the 3D flow of the kite. The study investigates the influence of parameters such as Reynolds number, leading edge radius, influence of canopy attachment and also considers the influence of fairing (curvature) of the canopy. For this 2D validation study the influence of Reynolds number and leading edge radius will be investigated [29].

A structured O-grid approach is used to generate a mesh around the geometry as it is easy to generate and produces a mesh of high quality as can be seen in Figure 4.2. A case is run with a d/c ratio of 0.083, at α of 2 and 10 degrees to understand the flow pertubations caused by the splitted plate in stalled and non-stalled conditions. One can visualize the flow behavior in Figure 4.3. As mentioned in section 3.1.2, the flow for the kite will include attached flow on the suction side with high pressure gradient. While on the pressure side there will be separation induced due to the bluff leading edge. This hypothesis on the flow behavior is seen to be reciprocated for the splitter plate as shown in Figure 4.3. It is seen that on the pressure side, flow behind the leading edge is highly turbulent and leads to the formation of vorticies. The flow is seen to reattach to the plate following this vortex. In the stalled case where α is 10 degrees, one can see flow separation on the suction side which leads to stall.

Before looking at specific cases it is critical to ensure that the mesh is accurately modelling the flow and that the results are accurate. A mesh convergence study with a d/c ratio is conducted by varying the number of points used to represent the kites shape. It is important to note that the Reynolds number in the reference uses a Reynolds number, which is constant with respect to the diameter Re_d. When converting to the sections Reynolds number (Re_c) one has to multiply this parameter by the

diameter to chord ratio (d/c), leading to the usage of different Reynolds numbers for the simulations. The results of this analysis can be seen in Figure 4.4. As one can see the results are largely unaffected by the number of cells used to represent the object (minimal variation between 400 cell points and 900 cell points), it is therefore sufficient to use a mesh with 400 points to model the kite. But the results do vary significantly from the reference. As the reference study used has not been published there is a lack of clarity on whether the variations are due to the setup of the simulation or with the experimental setup. Possible errors in the experimental setup include improper definition of the surface area, improper chord line definition, different turbulence parameters etc.

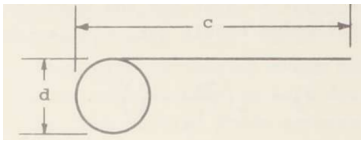

Figure 4.1: Splitter plate shape

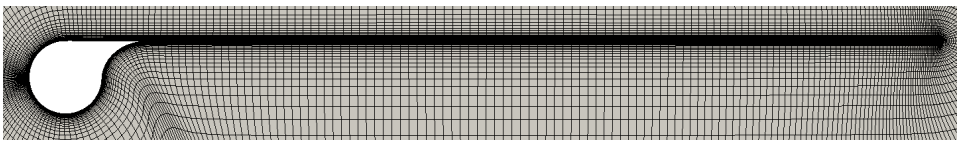

Figure 4.2: Splitter plate mesh, (case: d/c = 0.083, 400 points)

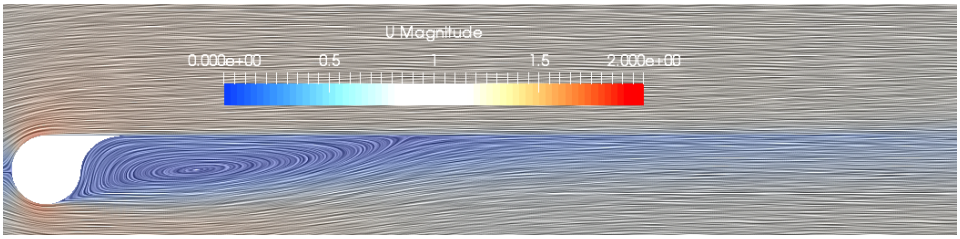

(a) α=0 deg

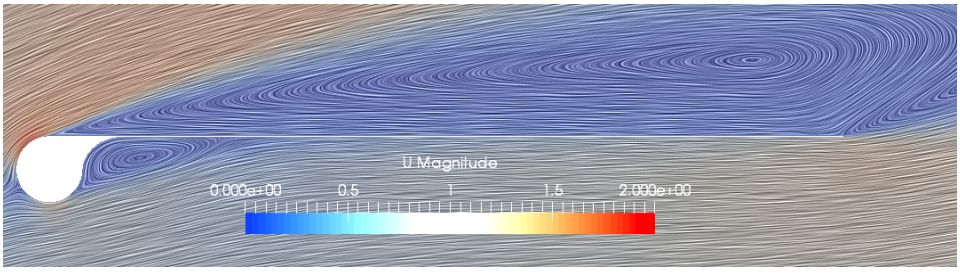

(b) α = 10 deg

Figure 4.3: Splitter plate velocity contours, (case: d/c = 0.083, Re_d=4.95×10^5)

The author of the paper could have considered multiple options for the definition of the surface area. Whilst the general method involves the usage of the chord length (S_c) as the surface area (used for airfoil analysis, and in the comparison), it is possible that this convention may not have been used depending on the goal of the analysis. If the focus of the study was to investigate the resistance to the flow the study may have considered the frontal area (S_f) when defining the surface area. If the focus of the study was to investigate the friction between the body and air the study would consider the total (wetted) surface area (S_wetted) [35]. The impact of these potential variations can be visualized in Figure 4.5. As can be seen the slope of the experimental results closely resembles the convention of wetted surface area. It is still seen that the measured results are off by an angle of approximately

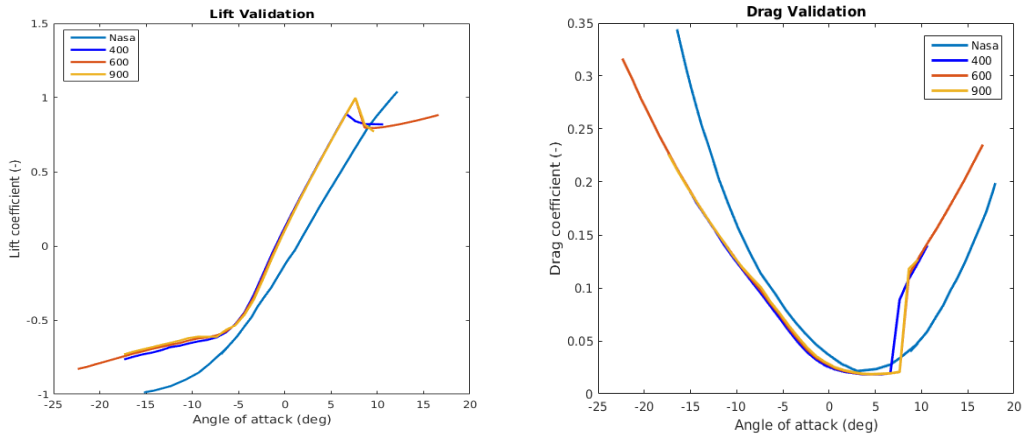

(a) Lift coefficient (b) Drag coefficient

Figure 4.4: Influence of grid points representing splitter plate on accuracy of results (case:Re_c=6×10^6, d/c=0.083)

2.5 degrees. One can hypothesize that this might be due to improper definition of the angle of attack, wherein it is measured with respect to the top line rather than the chord line. If one applies this condition as can see in Figure 4.5, the accuracy of the results is very good except for in stall.

Whilst the potential errors in the reference do address the deviation at low angle of attacks, the simulation still predicts stall to occur at a lower angle of attack. It is important to address the limitations of the simulation and assess whether these limitations might be affecting the accuracy of the results. The results could be improved by adding a transition model. Initially, as the flow over the geometry is not perturbed it can be considered to be laminar. However at high angle of attacks due to adverse pressure gradients as one moves towards the tip, the velocity at the boundary of the kite slows down leading to turbulence and ultimately separation. By adding a transition model, one can recreate the initial behavior where the flow is laminar and is transitioning to turbulence thereby increasing the accuracy in flow development over the splitter plate. In order to estimate the effect of a transition model one can look at reference [30] which looks at the impact of a transition model on a high Reynold number simulation of a 2D cylinder and [31] which looks at the influence of a transition model for flow over a flatplate. For the splitter plate one notices flow separation at the leading edge pressure side, from reference [30] one can see that by adding a transition model to the $k-\omega$ SST model the flow separation is delayed for the pressure side of a circle. Furthermore in accounting for stall behavior at the suction side one can look at reference [31], this study looks at the impact of a transition model on flow over a flat plate. It is seen that by adding a transition model to the $k-\omega$ SST model the separation over a flat plate is delayed. The results are confirmed by comparison studies carried out on varied shaped airfoils [3]. Other deficiencies in the model include the FVM schemes ability to model flow vorticies, as the simulation uses an upwind scheme it cannot effectively address flow reversals in the vorticies. Furthermore as the study uses a steady-state RANS simulation it cannot effectively model flow separation especially at the pressure side which is highly time dependent. Whilst it is possible that by making the mentioned adjustments to both the model and by estimating the errors in the reference study one will be able to attain results that better recreate the results of the study, by doing so one would have a confirmation bias. It would be advisable to redo the experiment in a controlled environment to make assertive statements on the validity of the model.

The kite´s sectional geometry includes a circular leading edge followed by a curved canopy. The radius of the leading edge and the length of the canopy are varying along the span of the kite. It is therefore important to understand the implications of varying the d/c ratio on the results. As mentioned the leading edge acts like a bluff body which pertubates the flow behind it, by increasing the size of the leading edge one would therefore have greater pertubation and larger scales of vorticies being formed in the wake. Also as the scale of the leading edge is larger the curvature of the body will be lower leading to a lower adverse pressure gradient and therefore a delay in stall. This effect can be seen in Figure 4.6, where there is no separation on the suction side when the kite is simulated at an α of 10

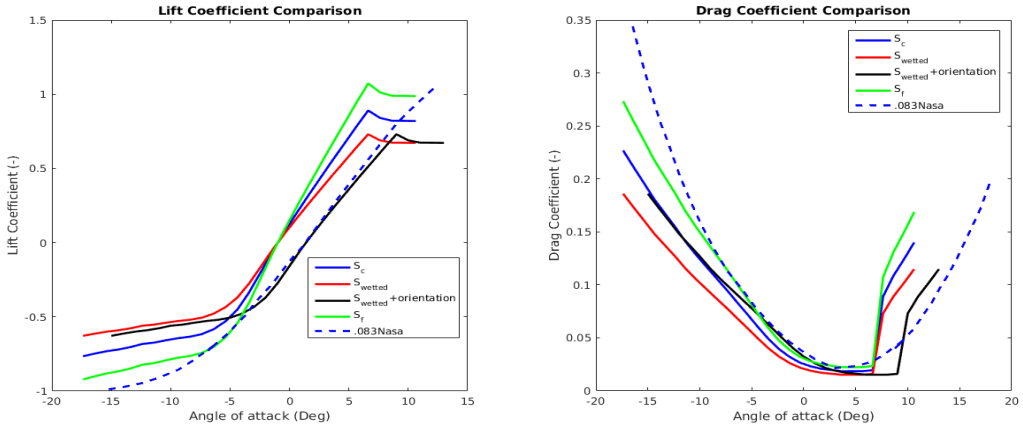

(a) Lift coefficient (b) Drag coefficient

Figure 4.5: Influence of surface definition on aerodynamic parameters (case:400 points, d/c=0.083, Re=6×10^6)

degree. One would therefore expect a delay in stall.

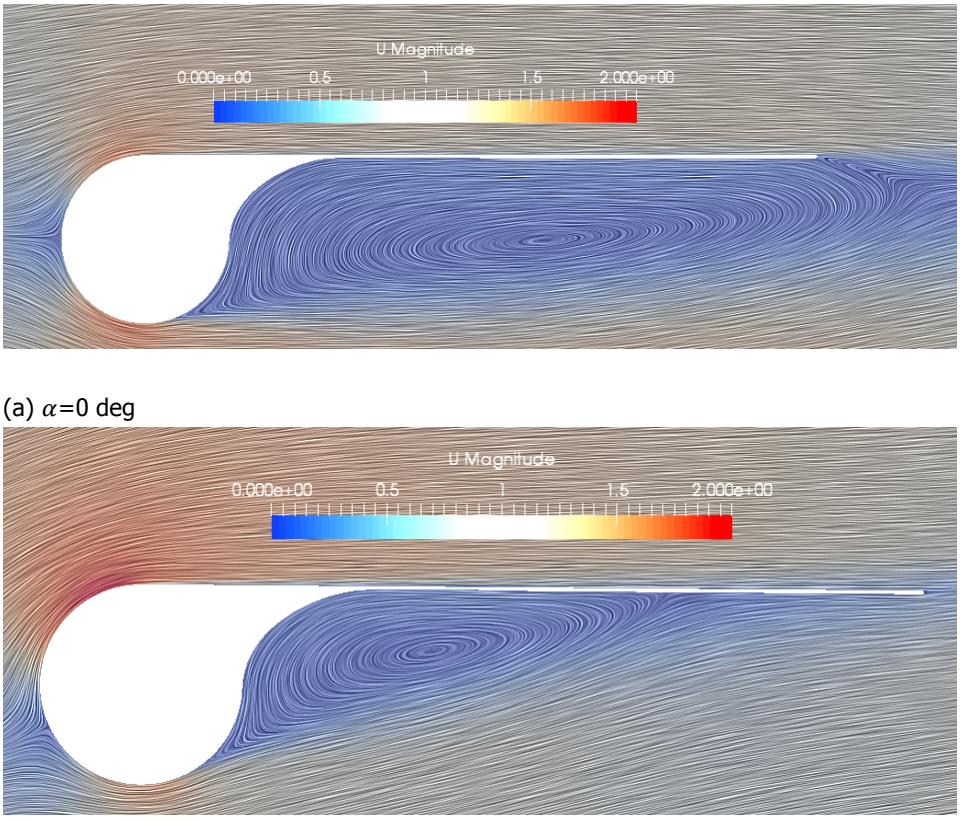

(a) α=0 deg

(b) α = 10 deg

Figure 4.6: Splitter plate velocity contours, (case: d/c = 0.222, Re=6×10^6)

One can validate the results with different d/c ratios in Figure 4.7. It can be seen that the results are more accurate for a smaller d/c ratio. This suggests that accurately modelling the turbulent flow oscillations in the wake of the leading edge is a challenge for this method. A possible reason why the model is unable to accurately model the turbulent flow in the wake of the leading edge is that the

method uses an upwind differencing scheme, which is not accurate at predicting the flow reversals that make up the vorticies. The errors concerning a large d/c ratio are not relevant to kites, as the sectional diameter to chord ratio (d/c) of kites is approximately 0.1 as shown in Table 4.1.

The final variable that will be addressed is the Reynolds number. This parameter determines the ratio of the inertial forces to the viscous forces. If one decreases this value, it would mean that there is a greater impact from the viscous forces. These viscous forces oppose the flow direction in the form of friction. Therefore for a case of lower Reynolds number one would expect stall to be at a lower angle of attack. One can confirm this with the results of this analysis presented in Figure 4.8.

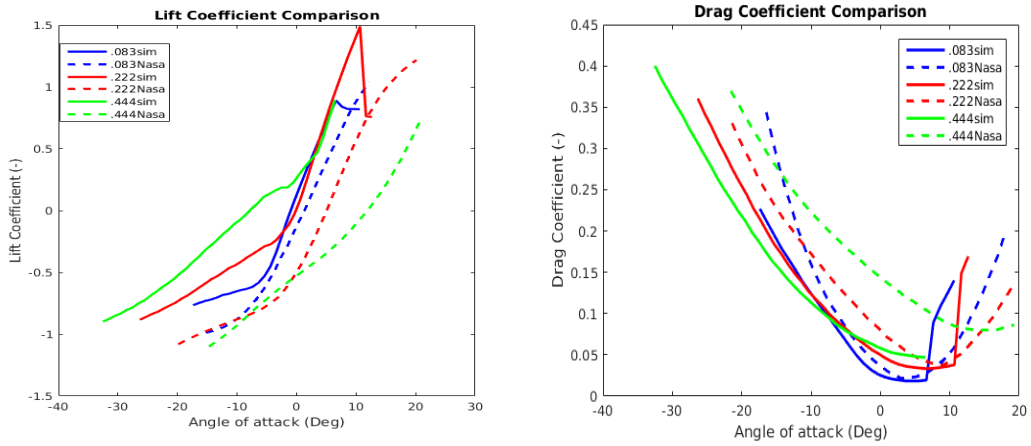

(a) Lift coefficient (b) Drag coefficient

Figure 4.7: Influence of d/c ratio on aerodynamic parameters (case:Re=6×10^6, 400 points)

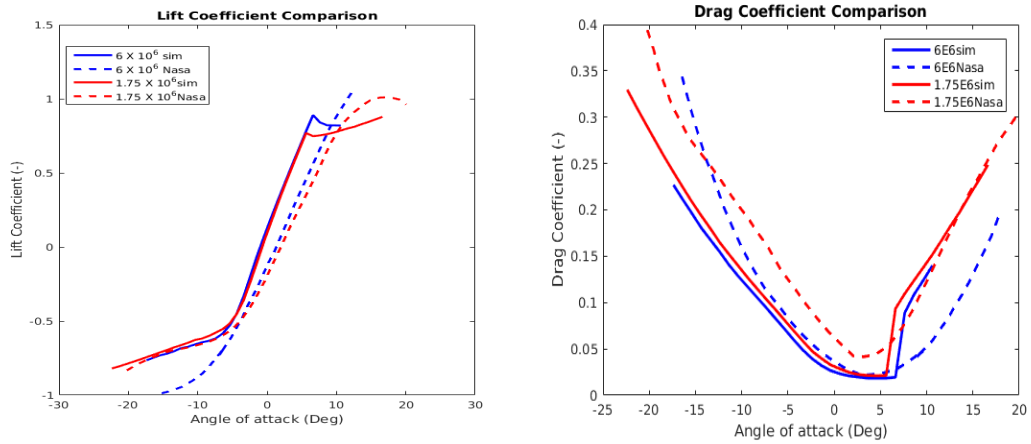

(a) Lift coefficient (b) Drag coefficient

Figure 4.8: Influence of Reynolds number on aerodynamic parameters (case:400 points, d/c=0.083)

4.2. 3D Kite Results

In this section the 3D simulation results of the kite will be presented and analyzed. This will include the results of both the deformed and the non-deformed kite. The analysis will look at global aerodynamic parameters and sectional aerodynamic parameters.

4.2.1. Non-Deformed Kite

In order to assess the 3D kite aerodynamic properties the kite is initially run at multiple angle of attacks without any deformations. The angle of attacks are selected until stall is reached. There will be greater focus at higher angle of attack as the kite in TU Delfts AWE system operates at a high angle of attack. It will also be possible to compare the results with Deaves [15] to understand the influence of the adjustments made.

One can view the aerodynamic coefficients and compare them with that of Deaves [15] in Figure 4.9. One can use this to gain insight into the impact the different approach has on the results. Whilst Deaves focused on ensuring that the y^+ value was constrained to a value of 1, this study has focused on reducing geometry alterations. In order to assess the impact these boundary layer parameters have on the results one can compare it to a mesh with a smaller boundary layer height (the change has been expressed in section 3.2. As can be seen the results of Deaves [15] experience stall at an angle of attack of approximately 20 degrees whereas in this investigation it was shown to be at approximately 40 degrees. This stark contrast in results could be either from the improvements in the current simulation with regards to improving the kite geometry and limiting mesh quality issues. A counter argument can be made that the mesh used in the current study does not efficiently resolve the boundary layer; as the boundary layer generated has certain areas where the y^+ value goes to 4.5, whereas in the case of Deaves [15] this parameter was constrained to a value of 1. A further concern might be that the stall behavior is actually occurring at a later stage, this might be valid as the optimized mesh (which has a higher boundary layer height) has a delayed stall over the non-optimized mesh. The optimized mesh itself does not model the whole viscous layer and only considers flow that is 80% of free stream with the boundary layer. One can also see that the variation in results is quite minimal for lower angle of attacks, where there is no flow separation.

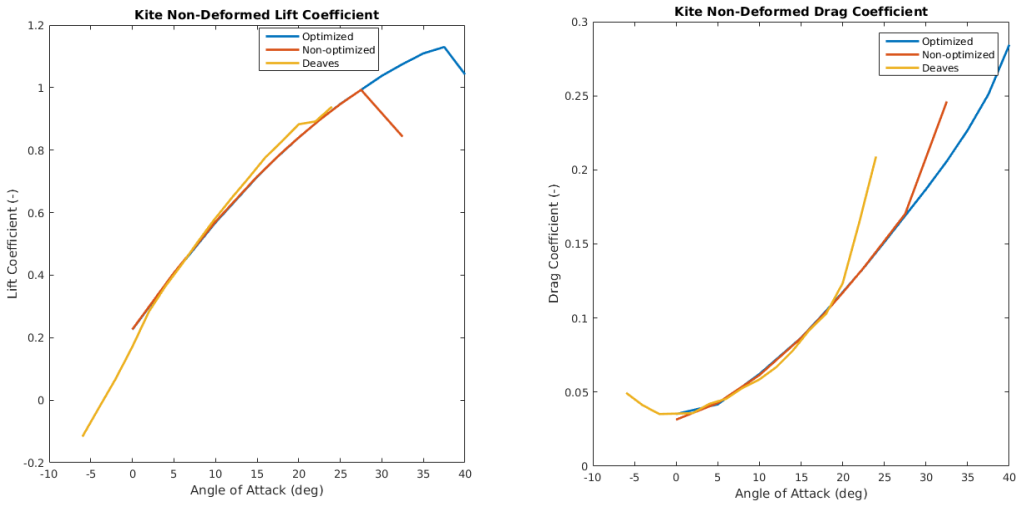

(a) Lift coefficient

(b) Drag coefficient

Figure 4.9: Aerodynamic parameters comparisons of Deaves, optimized and non-optimized kite without deformations [15]

To understand the 3D flow behavior of the kite a case without stall (α = 15 deg) and a case with stalled flow (α = 40 deg) are used. To understand the flow behavior glyphs representing the velocity vectirs are used to visualize the flow around the kite. The flow for the non-stalled case can be seen in Figure 4.10 where the arrow represents the direction of the flow and the colors represent the pressure. The flow behavior below the kite can be isolated by adding a pressure filter which filters negative values and the inverse can be done for the suction side. As can be seen the flow on the suction side is parallel to the flow direction, thereby indicating no stall. On the pressure side one can see that the flow aft of the leading edge is highly turbulent with significant flow reversal. It is however seen that at approximately 25% of the chord length the flow reattaches to the kite. Similar velocity vectors are generated for the stalled case (α = 40 deg) in Figure 4.11. It can be seen that the flow on the suction

side is oriented more towards the center of the kite. It is further seen that there is a formation of a vortex pattern near the mid of the kite. As the streamlines in the middle section of the kite is not aligned to the flow direction, the flow in this region has been stalled. These results do slightly deviate from those shown by Deaves, whereby stall is initiated at both the tip and the quarter span of the kite [15]. This variation in flow behavior could address the differences in stall angle for the two cases. On the pressure side it is now seen that the reattachment of the flow is initiated prior to the non-stalled case. This makes sense because the flow inclination leads to only a fraction of the flow being perturbed by the leading edge.

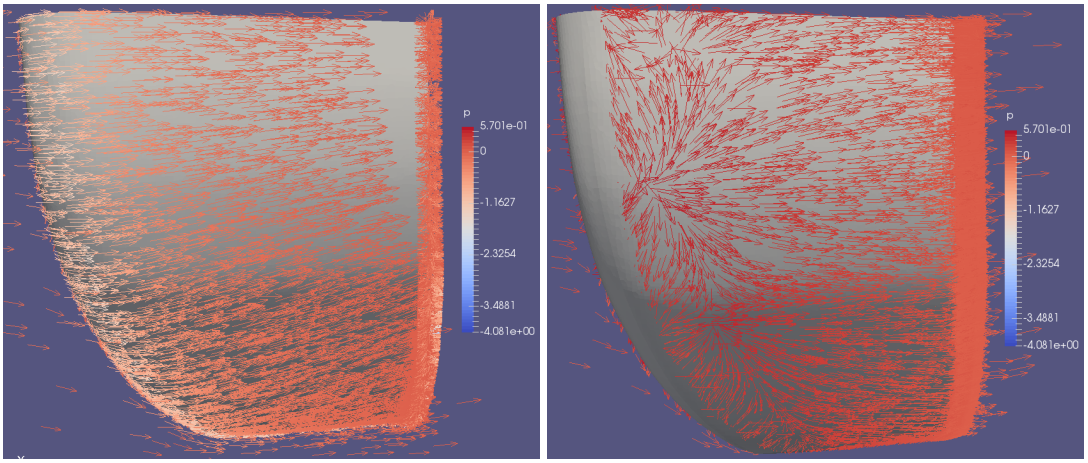

(a) Suction side (b) Pressure side

Figure 4.10: 3D velocity vectors of non-deformed kite for non-stalled flow at α=15

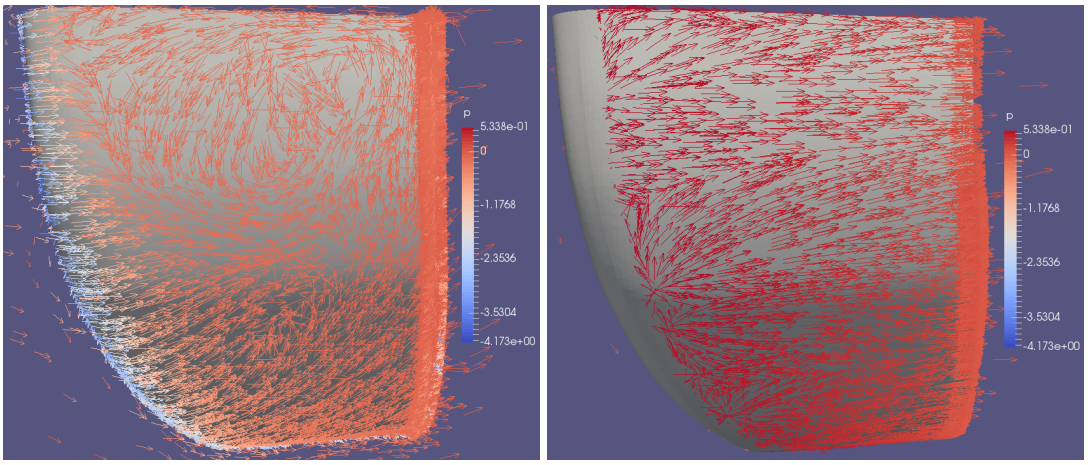

(a) Suction side (b) Pressure side

Figure 4.11: 3D velocity vectors of non-deformed kite for stalled flow at α=40

Breukels has used a 2D CFD study on the LEI kite sectional geometry as a basis for his aerodynamic model. It would be interesting to extend this to include the 3D flow effects. If one is able to quantify this influence and to understand its variance in the spanwise direction it would be possible to improve Breukels model [9]. It is expected that the results of the sectional study will be similar to that of the 3D study as the 3D aerodynamic parameters are essentially a sum of the sectional parameters (not for the aerodynamic coefficients as they have to include the effect of surface area).

In order to do this firstly the kite is separated into four sections as shown in Figure 4.12. A comparison of the section used for the 2D study can be compared with the sectional shape in Figure 4.13.

As can be seen the sectional shape of the kite has a higher curvature when compared to the splitter plate. This geometric variation is similar to a top fairing, as shown in [29]. [29] and [42] perform a comparative study to understand the influence this geometric alteration will have on the aerodynamic parameters of a para-wing with 50 degree sweep, this has been reproduced in Figure 4.14. It can further be seen that the 3D results when compared to the 2D section study has a delay of stall and an increase in lift and drag coefficients, similar to that seen in the global parameter analysis. It would be interesting to understand how the flow varies for the 3D section compared to that of the 2D sections and the impact this has on the resulting aerodynamic coefficients.

In order to understand how the flow varies along the span, the flow on section 1 and section 3 will be compared for an angle of attack of 15 and 40. The study will be useful to understand the influence of the kite's geometry and the implications it has on the flow. The analysis will further discuss the variations in flow behavior as one goes from a section in the middle of the kite to one near the tip. One can visualize the variations at an angle of attack of 15 degrees in Figure 4.15 and for 40 degrees in Figure 4.16. From Figure 4.15, it is possible to see that for section 1 (mid span) whilst the flow is turbulent in the wake of the leading edge there are no vorticies, which differs from the 3^{rd} section and from the non-stalled flow of the splitter plate. This difference in flow behavior is due to the lack of smoothing applied in the middle section when creating the kite geometry which causes the spanwise flow to converge and align with the flow direction. The flow on the suction side is similar for all cases with an attached boundary layer. One can view the results of the stall case,α = 40 degrees, in Figure 4.16. It can be seen that for section 1 the flow is highly separated on the suction side while for the 3^{rd} section the flow is still attached. One can therefore expect the stall to be initiated at the first section and gradually propagate spanwise. This behavior can also be observed by looking at the streamlines shown in Figure 4.11, at the location of section 1 there is significant flow reversal.

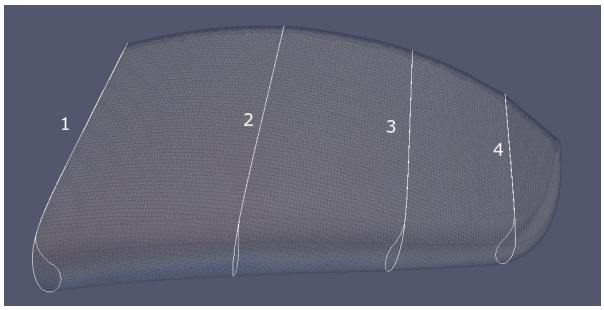

Figure 4.12: Discretization of non-deformed kite into 2D sections

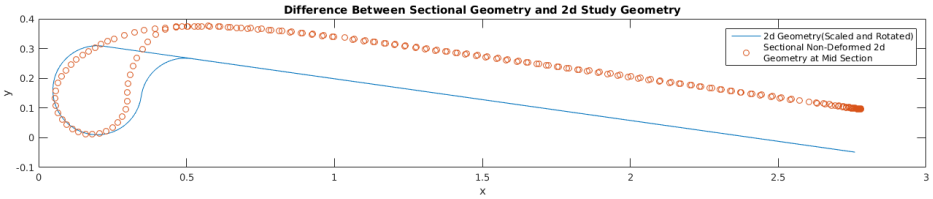

Figure 4.13: Difference between 2D sectional shape and 2D splitter plate

In order to determine the aerodynamic parameters for the local sections one has to firstly classify each section's d/c ratio, local twist (α_t) and anhedral angle (Γ), as shown in Table 4.1. One can then based on the cumulative pressure distribution compute the lift and drag of the section. For the drag one also has to also compute the friction drag due to the wall shear stress using equation 4.2 where τ_{w_N} is the component of the skin friction coefficient and c is the sectional chord length. One can now compare the computed aerodynamic coefficients with the associated 2D case from Figure 4.7 using linear interpolation to the required angle of attack and d/c ratio. The comparison is carried out for five key angle of attacks. The selected angles include 0, 5, 15 degrees to assess the 3D flow effects by comparing it to its equivalent 2D splitter's aerodynamic coefficients, and 30, 40 degrees to assess the influence of stall. The results of the comparison can be seen in Table 4.2, and illustrated

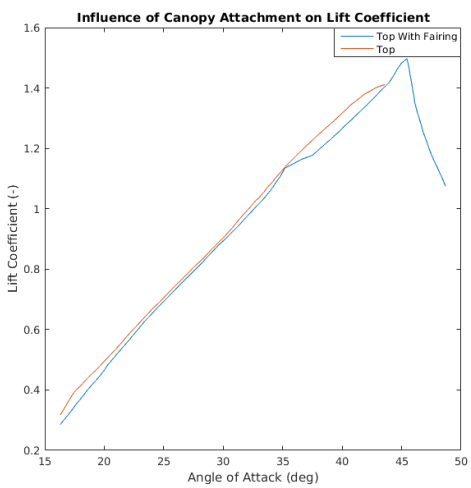

(a) Lift coefficient

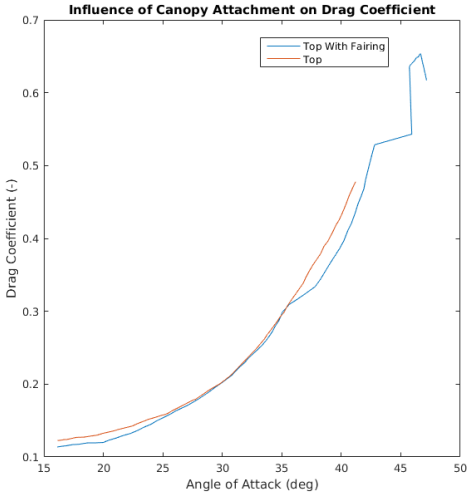

(b) Drag coefficient

Figure 4.14: Influence of curvature similar to Figure 4.13 on a para-wing's aerodynamic coefficients

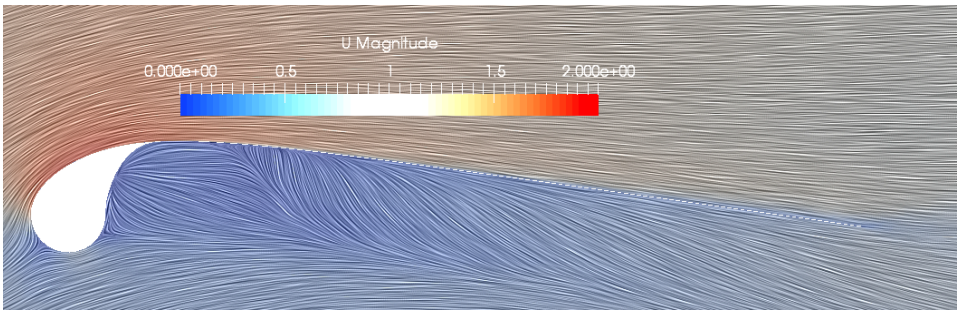

(a) Section 1

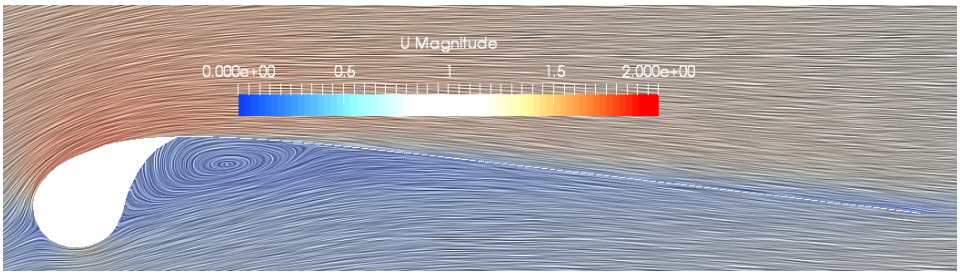

(b) Section 3

Figure 4.15: Sectional velocity contours of non-deformed kite at α=15

in Figure 4.17. One can see that although the 3D effects on the results cannot be easily quantified, the comparison shows that the 2D simulations have stall at much lower angle of attacks. Furthermore when comparing the different sections, it is seen that as one goes towards the symmetry plane the lift and drag properties of the sections increase for an equivalent angle of attack. This might be due to the spanwise flow towards the middle of the kite, seen in Figure 4.11 and 4.10. It can also be seen that the stall behavior at high angles of attack (40 degrees) initiates at the mid section, and as one moves from the symmetry plane it gets further delayed. This behavior is also seen in the 3D streamlines for the stalled case shown in figure 4.11.

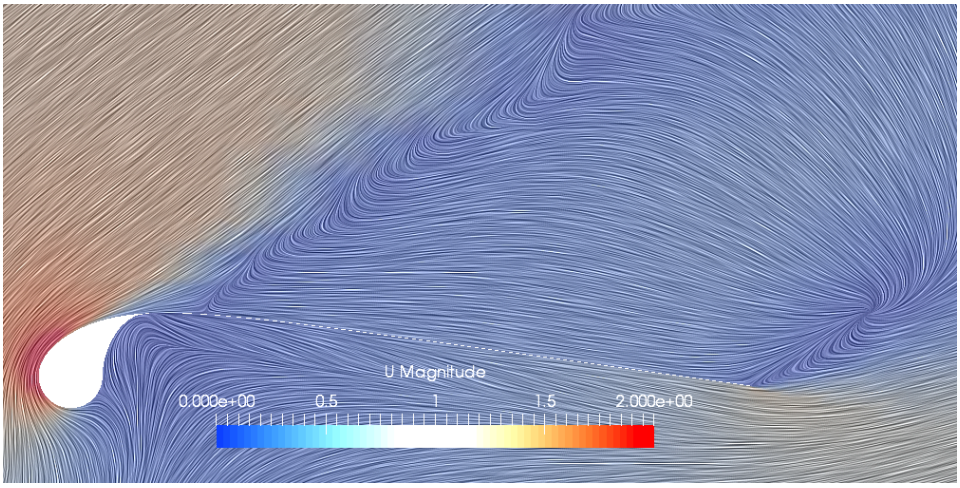

(a) Section 1

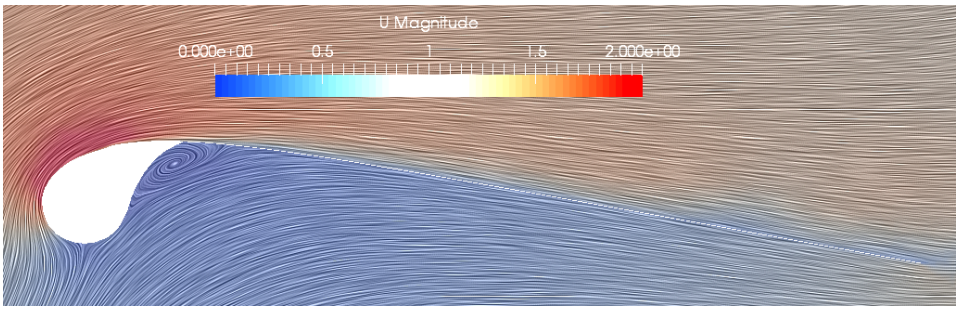

(b) Section 3

Figure 4.16: Sectional velocity contours of non-deformed kite at α=40

Table 4.1: Non-deformed kite sectional characteristics

Section	Spanwise Location(m)	c (m)	d/c	α_t (deg)	Γ (deg)
1	0	2.714	0.111	1.86	0
2	1.7	2.640	0.090	0.760	30.5
3	2.65	2.386	0.0997	0.192	55.2
4	3.12	1.96	0.127	0.614	72.5

$$c_l = \frac{L}{0.5\rho V^2 l} \tag{4.1}$$

$$c_{d_f} = \frac{\tau_w}{0.5\rho V^2 l} \tag{4.2}$$

4.2.2. Deformed Kite

The deformed shape as mentioned in section 3.3 involves an increase in the local angle of attack on the side of the turn and at this side the curvature of the kite in the spanwise direction had decreased and the opposite was true for the other side. Firstly this would cause a shift in the local sectional aerodynamics where the lift and drag on the side where the turn has been initiated would increase, and secondly due to local deformations it is expected that the global parameters would also decrease. The same global and local sectional analysis is extended for the deformed kite and carried out for the same angles of attack.

Table 4.2: Non-deformed sectional aerodynamic parameter compared with 2D simulations

α(deg)	Sec	C_l	C_d	$C_{l_{2D}}$	$C_{d_{2D}}$	α(deg)	Sec	C_l	C_d	$C_{l_{2D}}$	$C_{d_{2D}}$
0	1	0.362	0.0620	0.287	0.0370	5	1	0.674	0.0819	0.982	0.0339
	2	0.321	0.0827	0.113	0.0448		2	0.536	0.0719	0.856	0.0331
	3	0.174	0.0229	0.0505	0.0460		3	0.309	0.0387	0.772	0.0325
	4	0.095	0.0255	.1236	0.0392		4	0.131	0.0207	0.821	0.0291
15	1	1.17	0.176	0.741	0.252	30	1	1.60	0.346	-	-
	2	0.952	0.136	0.736	0.232		2	1.37	0.283	-	-
	3	0.546	0.0582	0.746	0.220		3	0.831	0.150	-	-
	4	0.225	0.0487	0.759	0.227		4	0.347	0.120	-	-
40	1	1.33	0.466	-	-						
	2	1.42	0.404	-	-						
	3	0.940	0.251	-	-						
	4	0.392	0.198	-	-						

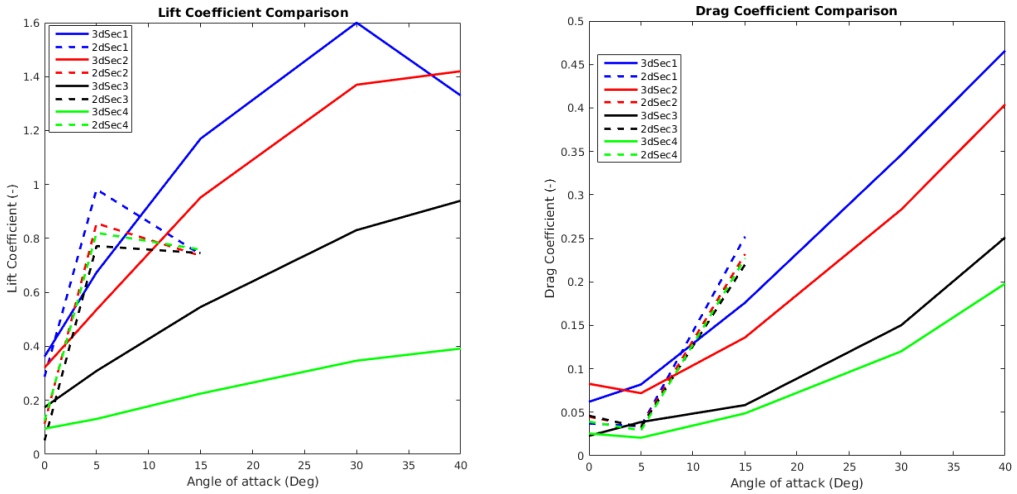

(a) Lift coefficient (b) Drag coefficient

Figure 4.17: Comparison of aerodynamic coefficients of 3D sections with equivalent 2D splitter plate

One can see the influence of the deformations on the aerodynamic parameters compared to a non-deformed kite in Figure 4.18. As can be seen the lift and drag are both reduced for the deformed mesh, but the stall angle is still the same. It is also possible to see that the curve of the deformed case is not as smooth as for the non-deformed case. Whilst the simulation was run for more iterations, based on these results the solutions is believed to not have converged. An analysis on the convergence criteria used and residuals for the kite for a deformed case one is referred to section 4.3.

For the case of the deformed kite it would also be interesting to analyze the moment coefficients which cause the kite to turn. In order to do this one has to first compute the center of mass. A rough estimate for this can be computed by looking at the mass breakdown of the kite and components center of gravity. For this computation two major components are used, namely the canopy and leading edge. The canopy includes the mass of the struts and sponsor logos. One can use the centroid of these local geometries to compute the centroid of the deformed kite on which the moment coefficients can be computed. The resultant moment coefficients can be seen in Figure 4.19. As can be seen from the results the curve is not smooth, one can therefore further assert that the flow has not effectively converged. The moment coefficient that is critical for the turning behavior is the yaw moment as mentioned in the introduction. This parameter increases beyond stall. It is therefore advisable for the smallest radius of a turn, thereby limiting the aerodynamic impact this has, one should fly at an angle beyond stall.

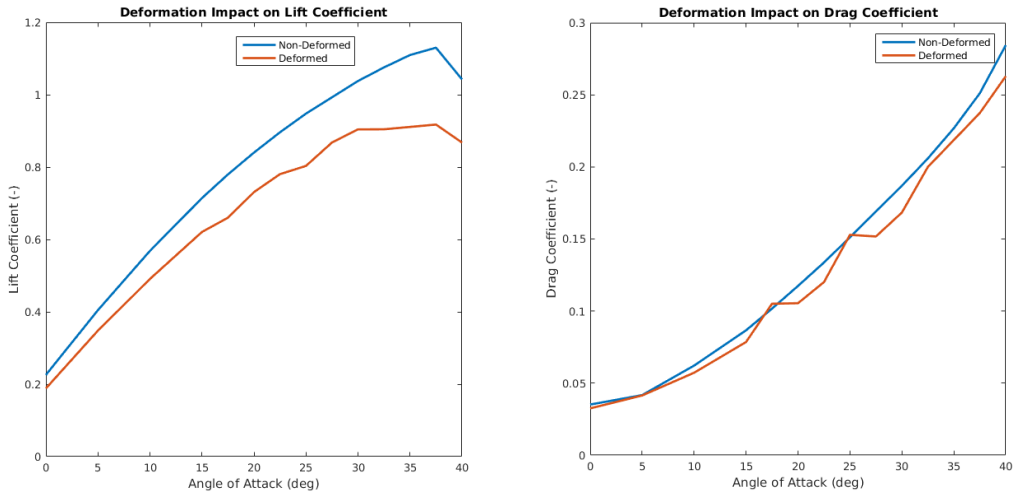

(a) Lift coefficient (b) Drag coefficient

Figure 4.18: Aerodynamic comparisons of deformed and non-deformed kite

It is possible to verify the adaptions to the kite's angle of attack for a turn in Figure 1.7, where side-slip angle is generally associated with an increase or decrease in the angle of attack.

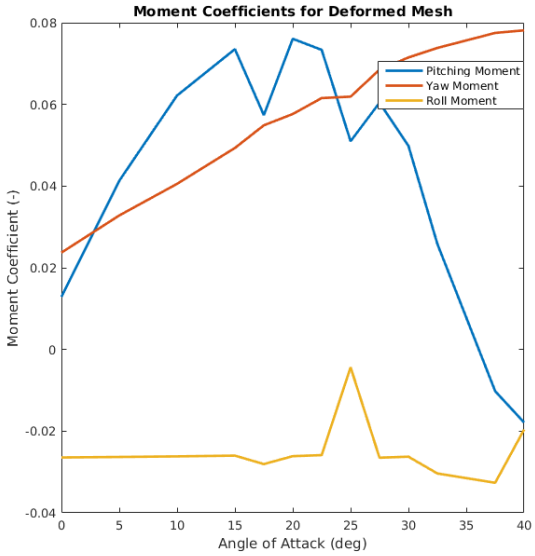

Figure 4.19: Moment coefficient associated with the deformed mesh

Whilst the stall behavior of the kite initiates at the same angle it would be interesting to assess how and on which side it develops. In order to do this the flow behavior of a non-stalled case with α of 15 degrees will be compared to that of a stalled case with α 0f 40 degrees, similar to the process carried out in the non-deformed study. One can visualize the streamlines for the non-stalled case in Figure 4.20. It can be seen that the streamlines at the suction side are all pointing in the streamline direction and are inclined towards the mid section of the kite. On the pressure it can be seen that the flow is similar to that of the non-deformed case, where initially there is high turbulence followed by reattachment. One can visualize the stalled case in Figure 4.21. It can be seen that on the suction side the streamlines are pointing towards the mid section, near the middle of the section the direction of the streamlines are scattered. One should therefore expect flow in this region to be stalled.

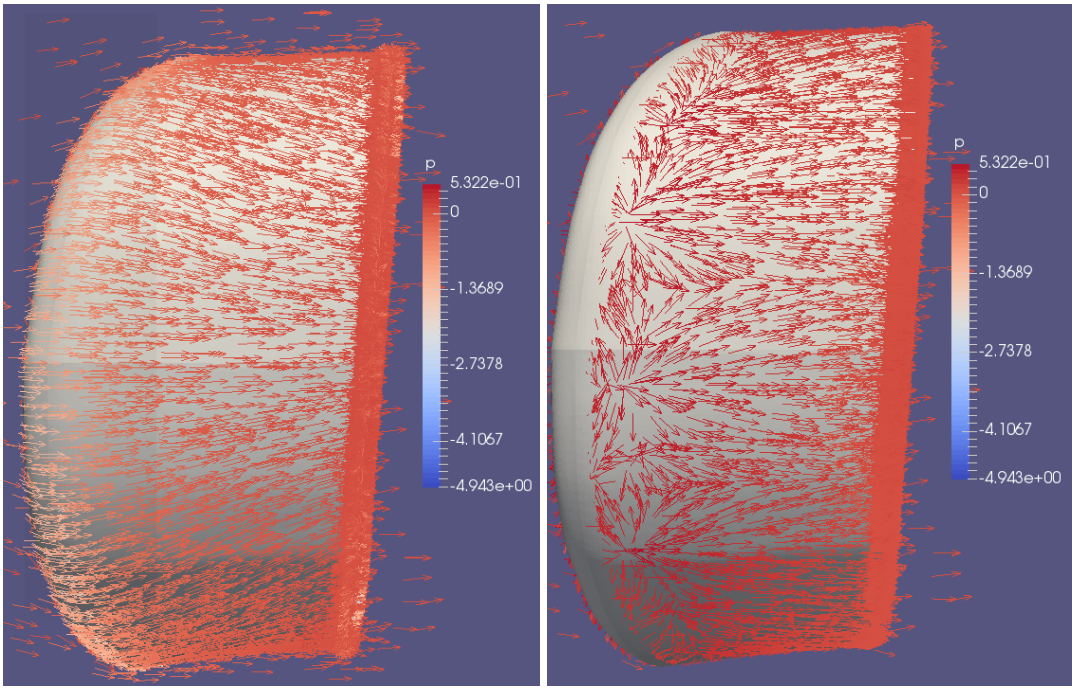

(a) Suction side (b) Pressure side

Figure 4.20: 3D velocity vectors of deformed kite for non-stalled flow at α=15

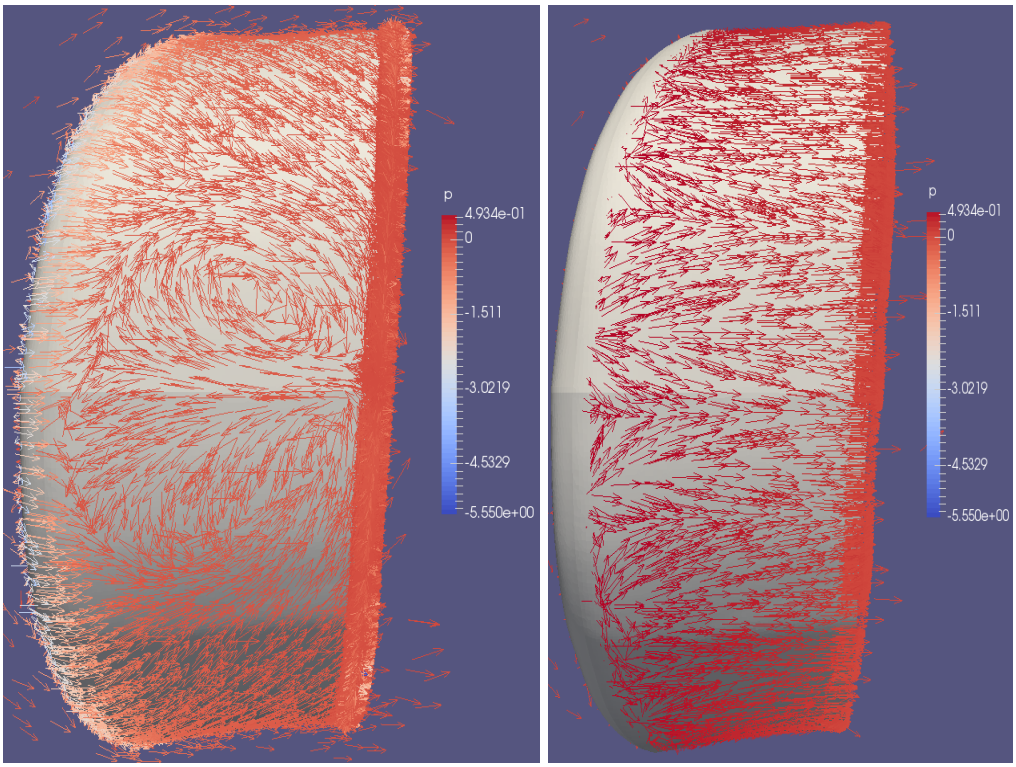

(a) Suction side (b) Pressure side

Figure 4.21: 3D velocity vectors of deformed kite for stalled flow at α=40

A sectional study will be conducted to assess if the stall behavior for the deformed model also initiates at the mid-span and if the sectional coefficients are incrementally lower as one moves towards the tip of the kite. It is important to know that the sectional shapes for the deformed case do not conform to any shape due to local deformations. It is however interesting to see the influence of these local deformations on the local aerodynamic coefficients and see how these local deformations effects the flow behavior. One can see the sectional distribution both on the right hand side (where the steering line is pulled) and the left hand side in Figure 4.22. It will be interesting to compare the flow behavior between the non-deformed and deformed case and see the impact the deformations will have on the flow behavior. In order to do this a sectional flow analysis at an α of 15 and 40 for sections 1, 3 and 6 will be conducted. One can visualize the flow behavior for the non-stalled case in Figure 4.23 and for the stalled case in Figure 4.24. It can be seen that for the non-stalled case there are flow vorticies formed on the pressure side of the kite for all sections. As shown with the streamline, the flow on the pressure side reattaches, after the initial turbulence. On the suction side the flow is attached throughout. In the stalled case however it is seen that on the suction side there is significant flow separation for section 1 only. This confirms the assertion of the fluid flow, which showed how the streamlines were only turbulent for the mid section (with flow reversal).

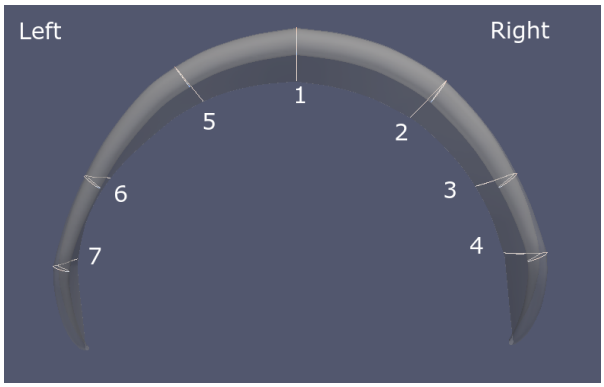

Figure 4.22: Discretization of deformed kite into 2D sections

One can now repeat the sectional analysis as was done with the non-deformed case to get the geometric parameters, shown in Table 4.3 and aerodynamic parameters, presented in Figure 4.25 for each section at the required angles of attack. The angle of attacks selected are the same as those for the non-deformed case. One can see that as one moves in a spanwise direction the aerodynamic forces of the sections gets reduced. When comparing the sections on the right (side where control line is pulled e.g. section 7) to those on the left (e.g. section 4) one sees that the drag coefficient is incrementally lower for the right side as the angle of attack increases. The lift is also lower for the right side but the difference is constant. The yaw moment is caused by the difference in drag and the offset in lift (this is subject to change as the orientation of the force vectors changes with angle of attack). Furthermore one can see that similar to the non-deformed case, the stall behavior is initiated at the mid-section.

Table 4.3: Deformed kite sectional characteristics

Section	Spanwise Location (m)	c (m)	d/c	α (deg)	Γ (deg)
1	0	2.708	0.0895	3.51	0
2	1.65	2.59	0.0907	2.722	36.9
3	2.5	2.38	0.0946	0.7449	53.1
4	2.95	2.11	0.122	0.6517	66.3
5	-1.34	2.63	0.0871	1.68	36.9
6	-2.5	2.40	0.0962	-2.555	53.1
7	-2.95	2.00	0.132	-1.23	72.5

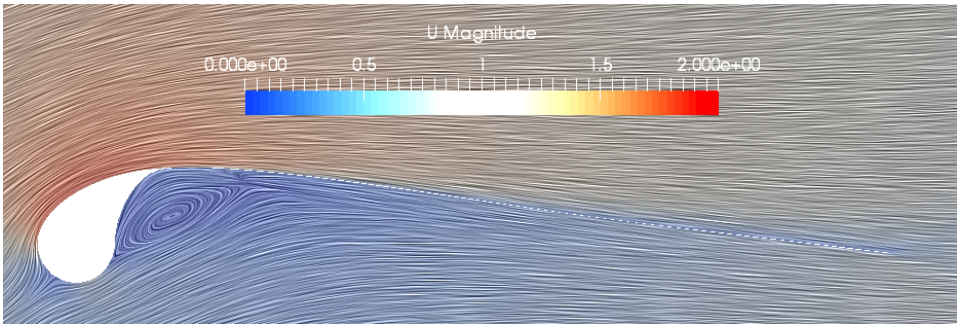

(a) Section 1

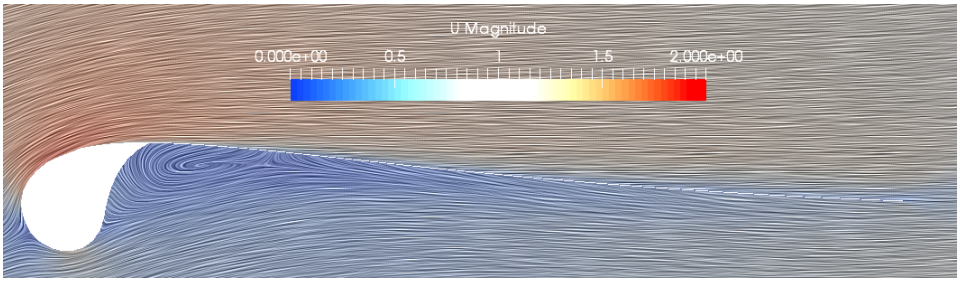

(b) Section 3

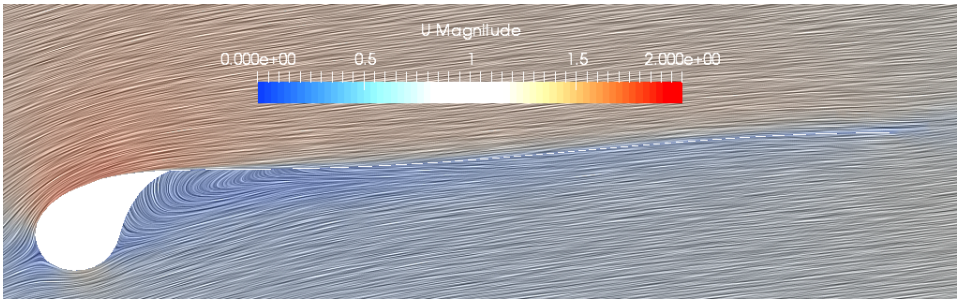

(c) Section 6

Figure 4.23: Sectional velocity contours of deformed kite at α=15

4.3. Convergence

Convergence of a solution is an indicator of the stability of the solution and its reproducible nature. Convergence looks at ensuring that residuals including velocity, pressure, turbulence parameters and pressure coefficients reach a stage where fluctuations and margin of error is minimal. The residuals indicate the local imbalance of the conserved variable in the flow domain. This section will look at the convergence of the 2D splitter plate as well as the 3D simulations of both the non-deformed and deformed kite geometry.

The convergence of a simulation is largely governed by the finite volume schemes, the relaxation parameters, the flow behavior and last but not least the mesh size and quality. Due to differences in the quality of the mesh one has to set different criteria's for each simulation setup. Whilst it is possible to set strict convergence criteria's in the solution parameters when running the simulation; meeting the standards set is not always possible due to the unsteady nature of the solution. This is especially true for cases with high turbulence and flow separation, where reaching a stable solution is extremely difficult and associated with a high computation cost. One therefore has to make an assessment of accuracy of simulation against computation time.

One can set a criteria on either the flow residuals or on the resulting force coefficients. One has to ensure that the flow variables have converged to a scale where the influence on the force coefficients

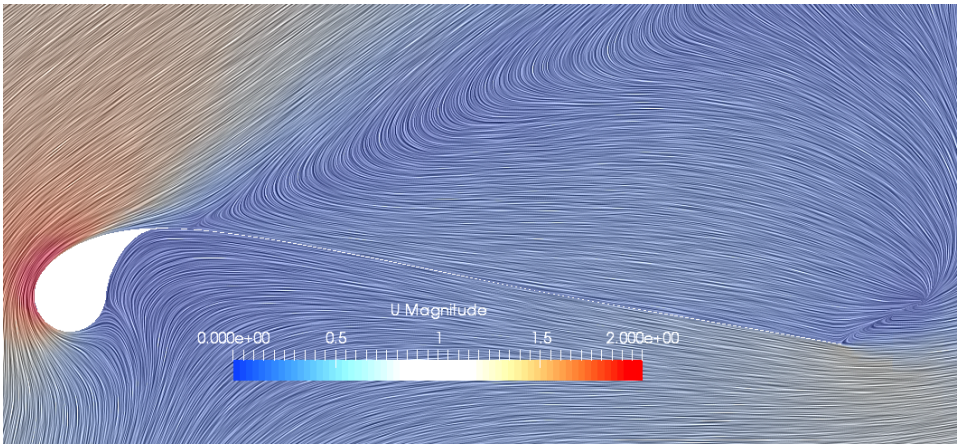

(a) Section 1

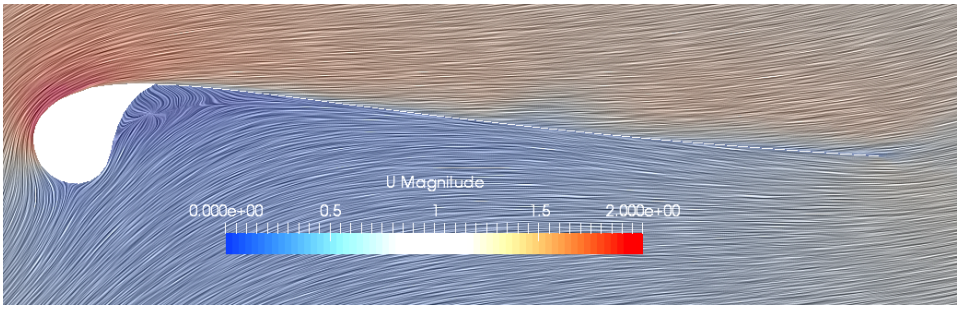

(b) Section 3

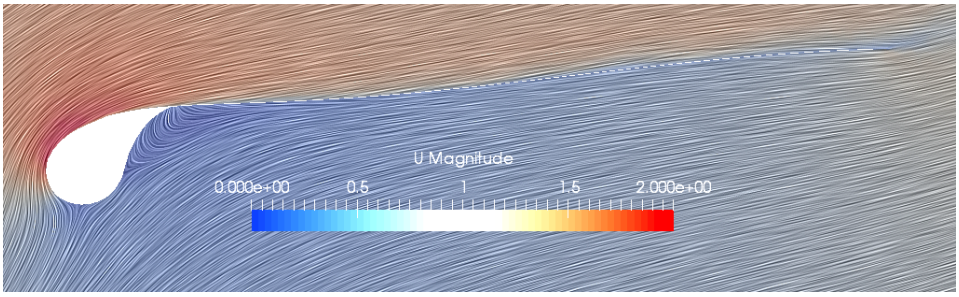

(c) Section 6

Figure 4.24: Sectional velocity contours of deformed kite at α=40

is minimal. In the case of 2D, as it is a structured high quality mesh it is possible to set a very strict criteria. Criteria's are set by looking at the residuals for the cases that are most critical, i.e cases where stall behavior is prevalent. One can see the variation of the force coefficients and residuals for a 2D case where stall is prevalent in Figure 4.26. As can be seen for this case although the flow behavior is extremely complex with separation and vortices the forces converge after 1500 iterations. Furthermore with regards to the flow residuals they reach approximately $10^{-}6$ with limited fluctuations thereafter. When analyzing the data, the initial fluctuations are not considered by computing the aerodynamic parameters by averaging the results of the simulation of the last 500 seconds.

The same approach is carried out for the 3D cases. In these cases due to the increased complexity of the simulation, it is increasingly difficult to reach a converged solution. The approach used will look at ensuring that the flow residual converge and reach a stage where they have minimal fluctuations. One can see the convergence of the solution for an angle of attack of 40 degrees (with stall) in Figure 4.27. Whilst it is not possible to visualize the variations in force coefficients, it is assessed to be limited

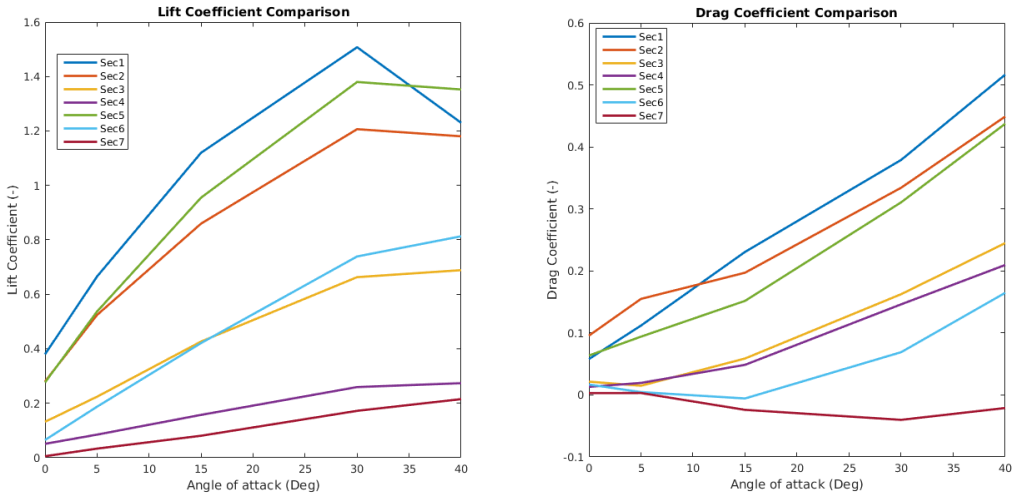

(a) Lift coefficient (b) Drag coefficient

Figure 4.25: Comparison of aerodynamic coefficients of 2D Sections for a deformed kite

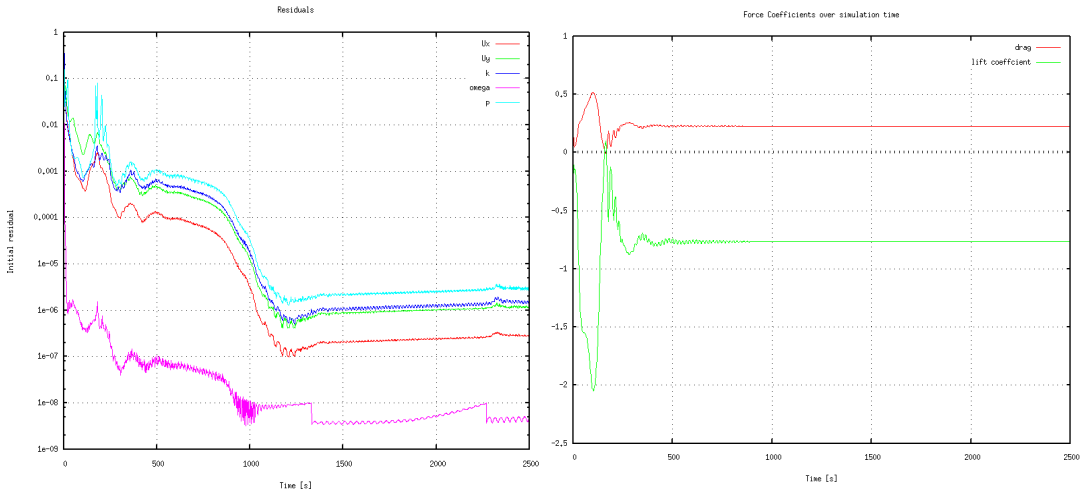

(a) Flow residuals (b) Force components

Figure 4.26: Flow convergence of 2D splitter plate, case:d/c=0.083,Re=6×10^6,α=15deg

to the scale of 10^-3 for the last 1000 seconds. As for the flow residuals one can see that apart from the spanwise velocity which has residuals of approximately 10^-5, the flow variables are highly converged with residuals in the order of 10^{-6}.

One can repeat the analysis for the deformed mesh. One can see the convergence of the solution for an angle of attack of 40 degrees in Figure 4.28. The data presented shows the results of the last 400 seconds so one can visualize local fluctuations in the force coefficients. As can be seen the residuals for each conserved parameter except for the spanwise velocity converges to the order of 10^{-6}. Also in the case of force coefficients there are local variations in the order of 10^{-3}, which is similar to that of the non-deformed case.

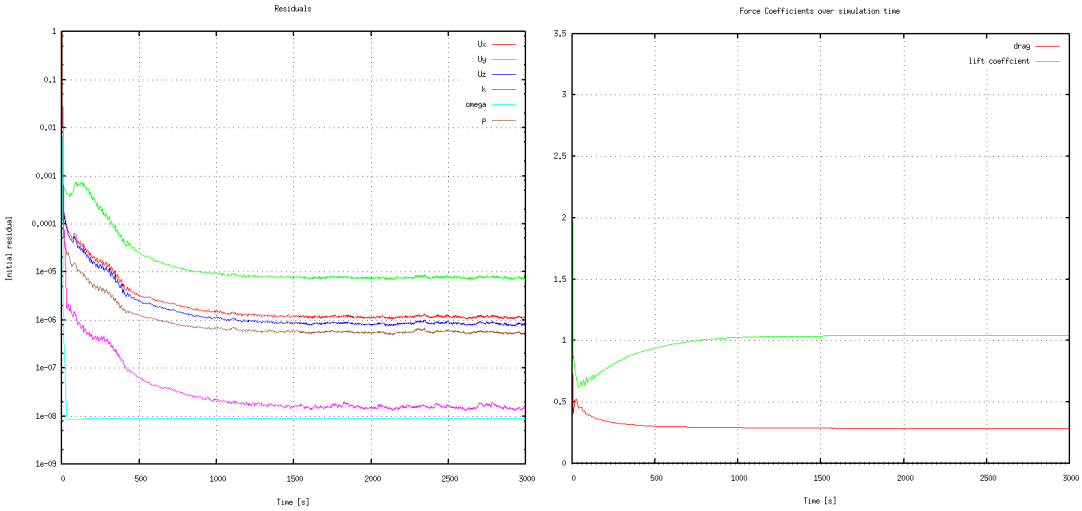

(a) Flow residuals (b) Force components

Figure 4.27: Flow convergence of 3D non-deformed kite at α=40deg

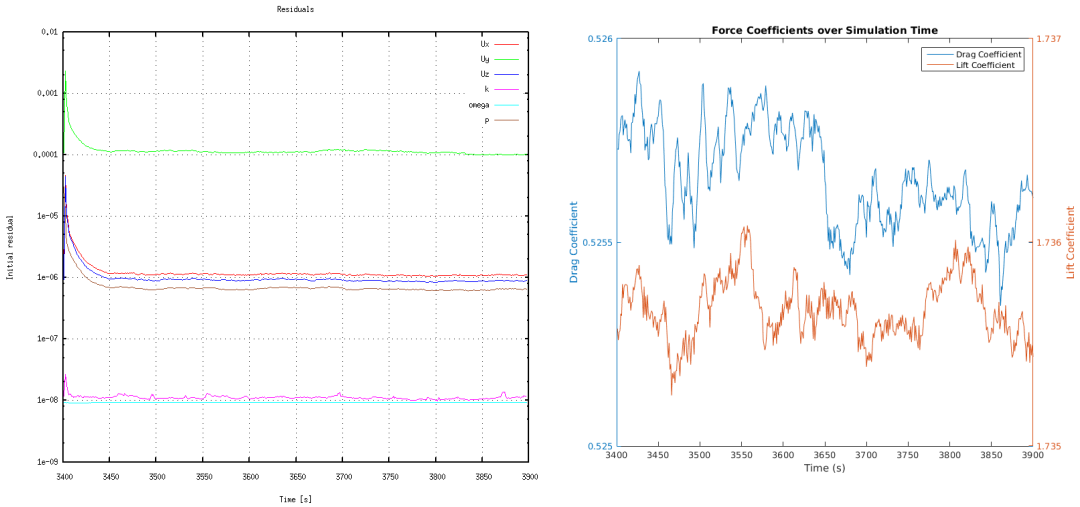

(a) Flow residuals (b) Force components

Figure 4.28: Flow convergence of 3D deformed kite at α=40deg

5

Conclusion and Recommendation

This thesis attempts to fill a knowledge gap regarding the performance of a kite when turning. To accomplish this goal the research performs a Steady State RANS simulation using OpenFOAM of the kite in both normal as well as turning orientation.

The thesis has three key objectives namely; generating a high quality mesh, understanding the impact of control-induced deformations and ensuring the approach is able to capture the flow dynamics of the kite.

The research details the approach used to trade-off geometry alterations with accuracy, whilst maintaining mesh quality and limiting computational cost. It builds on the work of Deaves [15] by improving areas which negatively impacted the aforementioned trade-offs. The resultant mesh involves a hybrid mesh with a structured boundary layer near the kite and an unstructured grid consisting of polyhedrals and tetrahedrals in the domain. There are still some deficiencies noted in the boundary layer parameters, with respect to the scale of the y^+ value and the boundary layer's ability to capture the complete viscous profile.

The assessment of the global aerodynamic parameters show that the stall of the kite occurs at an angle of approximately 40 degrees. This is significantly higher than the results obtained from Deaves's simulations [15]. The difference could be attributed to the changes in geometry. The results further show that stall behavior is initiated at the middle section and gradually moves towards the tips. This result also differs from the flow separation visualized by Deaves's simulations. The aerodynamic properties of a section as one moves away towards the tip get worse due to the increase in anhedral angle.

For the deformed state it is observed that sections on the side where the control input is applied have a higher angle of attack as presented by Bosch [8]. The kite loses its aerodynamic shape due to the deformations which results in a significant drop in the lift of the kite and a marginal loss on the drag. The turning behavior is primarily governed by the offset and difference in magnitude of forces at the tips. The delay in stall at the tips is reciprocated for the deformed case as well. This delay leads to the yaw moment increasing beyond the stall of the kite. It is therefore possible that one considers flying the kite in a stall configuration when performing a turning maneuver.

Validation studies with a 2D splitter plate are carried out to assess the methods capability of addressing the complex flow behavior of the kite. The significant accuracy issues observed in the simulations, could be due to the limitations of the method or errors in experimental setup. The flow behavior of the splitter plate and the kite's section were similar for most cases with vorticies and flow reattachment in the pressure side and attached flow for the suction side. Whilst the geometry was similar for the 2D splitter case and the kite's section, the aerodynamic parameters were not relatable. This difference was also observed in the reference study when the aerodynamic parameters of the 2D section was compared to that of a 3D planform.

The flow convergence was carried out on key aerodynamic parameters and residuals. The parameters converged to an acceptable level within a reasonable time frame. The aerodynamic parameters of the deformed mesh however indicate that the flow did not converge. This study does not cover the scope of visualizing flow separation on the kite accurately. Running the simulation for a longer period would be required to reach a completely stable solution and do this study. The results of the

While the RANS steady state method does require validation in being able to model effectively the complex flow behavior of the kite, its ability to address non linear flow effects within a limited time frame makes it a viable option for design optimization/system modelling.

In conclusion, this study has addressed the aerodynamics of the kite in both a normal and initial stage of a turn. Sufficient work still needs to be done in order to have a complete understanding of the flow behavior for all stages of operation. Addressing these new areas whilst improving the accuracy and validity of current models would allow for advancements in the field of kite design.

Recommendations

This section will cover the significant deficiencies in the approach and possible improvements one may consider going forward. Furthermore it will address ways in which research on the aerodynamics of the kite could be advanced.

In terms of meshing whilst the approach in this thesis was able to efficiently limit the geometry alterations considered in the work of Deaves [15], significant improvements can be made. These improvements could come in the form of understanding the influence of struts; whilst the effects of struts is hypothesized to be minimal aerodynamically it would be interesting to assert if this is the case. It would also be ideal to run a case where the canopy is represented by an infinitely thin surface, this approach would significantly reduce the number of cells and would increase the accuracy of results, unfortunately this was not possible with the chosen mesh tools. The issue of geometry alterations is also important in the case of the deformed model. The considered model does not efficiently resemble the geometry provided by Abaqus. It would be ideal, if this could be improved, by potentially adapting the deformed model using the same approach as that of the non-deformed case, thereby limiting changes in the general geometry.

In terms of mesh quality it would be ideal to have a mesh with a y^+ of 1 and a boundary layer height that completely captures the viscous sub-layer, whilst still maintaining or improving quality standards. This was deemed complicated with the model used, but could significantly improve the results of the simulation.

In terms of validating the approach. Due to significant differences when validating the 2D splitter case, it was not possible to validate the RANS approach for kite flows. One could look at repeating this process with the inclusion of transition modelling and/or recreate the experimental data of the splitter plate in a controlled environment.

When considering the turning of the kite, one would expect there to be a variation in the side-slip angle. While the current study does not consider this, by reasoning that the model is used when the initial control input is provided, it would be interesting to consider the influence this has on the aerodynamics of the kite.

One can look at improving the results of the deformed case by performing an iterative process where the results of the local parameter analysis from the CFD simulations are implemented into the Abaqus model. One can thereby perform an optimization process to get an accurate deformation. If possible it would also be advisable to iterate on the length of specific tethers to prevent sagging and simulate the behavior of pulleys on the bridle. It would also be useful to have additional iterations performed for the deformed kite, as the results indicate an unconverged solution.

The current simulation setup utilized the steady state solver (simpleFOAM) in OpenFOAM. This leads to inaccuracies in modelling dynamic flow behaviors such as flow separation, wind gusts, pitching moment etc. While it would be interesting to have a detailed unsteady analysis on these parameters, given the current tools and the current state of computational efficiency the computational cost of such an analysis would be extremely high.

Similarly when considering unsteady solvers in the case of deformations it would also be interesting to have a time based CFD simulation where one can visualize turning flight path, kite morphing into deformed state and variability in side-slip angle. These results will be useful in determining the ideal turning radius and thereby aid in the development of an ideal autonomous control system.

Convergence criteria is another area where there is a possibility of improvement. The results of the deformed kite seem to indicate that the flow has not converged and for the case of the non-deformed kite the current simulation runs for 3000s and is assumed to be converged. It would be interesting to run the current simulations for a longer period of time to improve the solution accuracy and stability of the solution. It would then be possible to assess the areas where flow separation is initiated.

Bibliography

[1] U. Ahrens, M. Diehls, and R. Schmehl. *Airborne Wind Energy*. Springer Heidelberg, 2013.

[2] J. Anderson. *Introduction to flight*. McGraw Hill, 5 edition, 2005.

[3] A. Aranake, V. Lakshminarayan, and K. Duraisamy. Assessment of transition model and CFD methodology for wind turbine flows. *AIAA Fluid Dynamics Conference and Exhibit*, 42, 2012.

[4] A. Arapogianni and A. Genachte. Deep water: The next step for offshore wind energy. Technical report, European Wind Energy Association, 2013.

[5] B. Ashari. Aerodynamic performance prediction of a tetrahedral kite. Master's thesis, Technical University of Delft, 2014.

[6] G. Balafas. Polyhedral mesh generation for CFD-analysis of complex structures. Master's thesis, Munchen Technical University, SOFiSTiK AG, 2014.

[7] J. E. Bardina, P. G. Huang, and T. J. Coakley. Turbulence modeling validation, testing, and development. Technical report, NASA, 1997.

[8] H.A. Bosch. Finite element analysis of a kite for power generation. Master's thesis, Technical University of Delft, 2012.

[9] J. Breukels. An engineering methodology for kite design. Master's thesis, Technical University of Delft, 2010.

[10] J. Breukels and W. Ockels. Design of a large inflatable kiteplane. *AIAA Structures, Structural Dynamics and Materials Conference*, 48, 2007.

[11] S.A. Carrillo. Cartesian grid generation. Master's thesis, TU Delft, 2013.

[12] J. Chawner. Quality and control – two reasons why structured grids aren't going away. http://www.pointwise.com/theconnector/March-2013/Structured-Grids-in-Pointwise.shtml, 2013.

[13] M. Chowdhury. The finite volume method: Basic principles and examples. Indian Institute of Technology Kanpur Lecture, 2009.

[14] S.G.C. de Groot. Modelling the dynamics of an arc-shaped kite for control law design. Master's thesis, Technical University of Delft, 2010.

[15] M. Deaves. An investigation of the non-linear 3D flow effects relevant for leading edge inflatable kites. Master's thesis, Technical University of Delft, 2015.

[16] U. Fechner, R. Vlugt, E. Schreuder, and R. Schmehl. Dynamic model of a pumping kite power system. *Renewable Energy*, 83, 2014.

[17] C. A. Felippa, K. C. Park, and C. Farhat. Partioned analysis of coupled mechanical systems. *Computer Methods in Applied Mechanics and Engineering*, 190, 1999.

[18] B.M.R. Franca. A tool for aerodynamic analysis of flexible kites. Master's thesis, Technical University of Delft, 2014.

[19] P.J. Frey. About surface remeshing. 9th International Meshing Roundtable, 2000.

[20] J. Guerrero. Introductory OpenFOAM course. http://www.dicat.unige.it/guerrero/oftraining/module0.pdf, 2015.

[21] L. Guo, A.R. Chen, and L.P. Xu. Strait crossing cable stayed bridge girder evolution. *Advanced Materials Research*, 250, 2011.

[22] K. Hirotsugu I. Toshio. *Kites: The Science and the Wonder*. Japan Pubns, 1 edition, 1983.

[23] International Energy Agency. World energy outlook 2015 factsheet. *Global energy trends to 2040:The energy sector and climate change in the run-up to COP21*, 2015.

[24] Kitepower.eu. Kite. http://www.kitepower.eu/technology/3-sytem-components/7-kite.html, 2016.

[25] Leap Australia: Computational Fluid Dynamics Blog. Turbulence part 3 - selection of wall functions and y^+ to best capture the turbulent boundary layer. http://www.computationalfluiddynamics.com.au. Accessed: 26/4/2016.

[26] M.L. Loyd. Crosswind kite power. *Journal of Energy*, 4, 1980.

[27] M.J. Lutton. Comparison of C-and O-grid generation methods using a NACA 0012 airfoil. Master's thesis, Air Force Institute Of Technology, 1989.

[28] P. McMurty. Length and time scales in turbulent flows. University of Utah Lecture, 2001.

[29] M.R. Mendenhall, S.B. Sprangler, and J.N.Nielsen. *Investigation of Methods for Predicting the Aerodynamic Characteristics of Two-Lobed Parawings*. Nasa, 1968.

[30] F.R. Menter, R. Langtry, and S. Völker. Application of the y-Reθ transition model to simulations of the flow past a circular cylinder. *Flow Turbulence Combust*, 97:97:401, 2006.

[31] F.R. Menter, R. Langtry, and S. Völker. Transition modelling for general purpose CFD codes. *Flow Turbulence and Combustion*, 77:77–277, 2006.

[32] C. Michler. Efficient numerical methods for fluid-structure interaction. Master's thesis, Technical University of Delft, 2005.

[33] C. Michler, S.J. Hulshoff, E.H. van Brummelen, and R. de Borst. A monolithic approach to fluid-structure interaction. *Computers and Fluids*, 33, 2003.

[34] V. Moureau, P. Domingo, L. Vervisch†, and D. Veynante. Dns analysis of a Re = 40,000 swirl burner. *Stanford Center for Turbulence Research Summer Program*, 2010.

[35] Nasa. Size effects on drag. https://www.grc.nasa.gov/www/k-12/airplane/sized.html. Accessed: 2017-06-05.

[36] Nasa. https://climate.nasa.gov/, 2016.

[37] OpenFOAM. Solution and algorithm control. http://www.openfoam.com/documentation/user-guide/fvSolution.php.

[38] OpenFOAM. OpenFOAM guide/the SIMPLE algorithm in OpenFOAM. https://openfoamwiki.net/index.php/OpenFOAM_guide/The_SIMPLE_algorithm_in_OpenFOAM, 2014.

[39] O. Pires, X. Munduate1, O. Ceyhan, M. Jacob, J. Madsen, and J.G. Schepers. Analysis of the high reynolds number 2d tests on a wind turbine airfoil performed at two different wind tunnels. *Journal of Physicss: Conference Series*, 749, 2016.

[40] Renewable Energy Network 21. Wind power markets. *Renewables 2015 Global Status Report*, 2015.

[41] J. Rhoads. How do you define a good grid? http://www.pointwise.com/theconnector/November-2014/What-Defines-a-Good-Grid.shtml, 2014.

[42] L. Rodger, Naseth, and T.G. Gainer. Low -speed investigation of the effects of wing sweep on the aerodynamic characteristics of para-wings having equal-length leading edges and keel. Technical report, NASA - Langley Research Center, 1963.

[43] M.B. Ruppert. Development and validation of a real time pumping kite model. Master's thesis, Technical University of Delft, 2012.

[44] H. Schlichting. *Boundary Layer Theory*. McGraw Hill, 1979.

[45] R. Schmehl W.J. Ockels S.G.C. de Groot, J. Breukels. Modelling kite flight dynamics using a multibody reduction approach. Technical report, Technical University of Delft.

[46] A. Sheffer, E. Praun, and K. Rose. Mesh parameterization methods and their applications. *Foundations and Trends in Computer Graphics and Vision*, 2, 2007.

[47] P.R. Spalart. Trends in turbulence treatment. Technical report, American Institute of Aeronautics and Astronautics, 2000.

[48] J.C. Stevenson. Traction kite testing and aerodynamics. Master's thesis, University of Canterbury, 2003.

[49] N. Timmer. Introduction to wind energy: Energy production. Technical University of Delft Lecture, 2014.

[50] United Nations. Framework convention on climate change; adoption of the paris agreement. 21st conference of the parties, United Nations, 2015.

[51] R. Verheul. personal communication.

[52] H.Y. Wong. A means of controlling bluff body flow separation. *Journal of Wind Engineering and Industrial Aerodynamics*, 4, 1979.